The Thermal Power Calibration of the SLOWPOKE-2 SMR

by

FADI AL ANID

A thesis submitted to the

Department of Physics, Engineering Physics & Astronomy

in conformity with the requirements for the

degree of Master of Applied Science

Queen's University

Kingston, Ontario, Canada

April 2025

Abstract

This thesis presents an experimental and computational methodology for accurately determining the thermal power output of the Royal Military College (RMC) SLOWPOKE-2 small modular reactor (SMR). Accurate determination of reactor thermal power is essential for calibration, fuel management, and compliance with International Atomic Energy Agency (IAEA) safeguards. Historically, the thermal power at RMC's SLOWPOKE-2 has been inferred from neutron flux measurements calibrated through older fuel configurations, potentially introducing systematic uncertainties post-refuelling.

Two complementary experimental techniques were developed to provide a robust and independent calibration. First, a controlled immersion heater assembly comprising two 1.5 kW single-phase heaters and one 6 kW three-phase heater was installed in the reactor pool. Five distinct power levels (1.5 kW, 3 kW, 6 kW, 7.5 kW, and 9 kW) were used to correlate measured thermal profiles, recorded by an eight-channel type-K thermocouple array, to the known heater power, establishing a reliable calibration constant ($\kappa = 1590 \pm 40$ °C·min^{-1}·kW^{-1}). This calibration yielded reactor power estimates systematically 10% – 20% higher than the control room's nominal reactor powers at similar neutron flux setpoints, indicating potential inaccuracies in existing reactor instrumentation.

Second, a heat balance method was implemented through Python, calculating power added based on measured temperature gradients from the thermocouple array, deionized water properties, and heat losses (convection, conduction, and evaporation). This method independently validated the calibration findings, estimating reactor power outputs similarly above nominal values, with uncertainties ranging between ±2% and ±10%.

Additionally, neutron flux data collected from B10+ and He-3 detectors before and after refuelling allowed for an analysis of the fissile isotopic changes. Using a power-to-ΔT correlation between reactor core inlet and outlet temperatures, a Neutron-Flux-to-Power Ratio was experimentally estimated using the B10+ and He-3 detectors, respectively. These values agree in magnitude with the weighted isotopic composition estimate at (-1.95%) by CNL using MNCP simulations, but differ in relative magnitudes before and after refuelling, highlighting potential model or experimental approximations.

Ultimately, these findings establish a dual-method approach for precise reactor thermal power calibration and provide preliminary insight that may support future improvements in fuel monitoring and proliferation safeguards.

Acknowledgements

First and foremost, I would like to express my deepest gratitude to my father, Khaled, whose unwavering support has been the foundation of all my academic achievements. From patiently answering my countless questions in school to making significant personal sacrifices as a civil engineer, he has truly shaped my opportunities and my passion for this field of learning. I'm also sincerely thankful for my amazing mother, whose loving support has provided me with the strength I needed throughout this journey.

I would also like to extend my sincere gratitude to my supervisor, Jordan Morelli, for his support throughout this journey, as well as my collaborators at Canadian Nuclear Laboratories (CNL), Dr. Bryan van der Ende, Dr. Justin Spencer, Dr. Krishna Podila, and Dr. Bhaskar Sur for their valuable guidance and support throughout our meetings. I am equally grateful to Dr. François Caron at the Royal Military College (RMC) for his ongoing mentorship. A special thanks is owed to Dr. Pavel Samuleev at the SLOWPOKE-2 facility, whose assistance with setting up and executing the experiments was essential to the success of this thesis.

Finally, I would like to express my heartfelt thanks to my family and friends for their unwavering support. Specifically, I feel incredibly grateful for my wonderful partner, Hannah, and her amazing parents and grandparents- Steve, MaryBeth, Pat, Pete (Chief), Shilagh, and Joseph. Their kindness, encouragement, and unwavering support over the past several years have truly meant the world to me.

Contents

List of Figures

List of Tables

Acronyms

AECL	Atomic Energy of Canada Ltd.
ANSYS	Computer-aided engineering simulation software
CAD	Computer-aided design
CANDU	CANada Deuterium Uranium
CFD	Computational Fluid Dynamics
CMC	Canadian Microelectronics Corporation
CNL	Canadian Nuclear Laboratories
CPM	Counts-per-minute
CRL	Chalk River Laboratories
IAEA	International Atomic Energy Agency
NRU	National Research Universal
RMC	Royal Military College
SIRCIS	SLOWPOKE Integrated Reactor Control Instrumentation Instrument
SLOWPOKE-2	Safe LOW-POwer (K)ritical Experiment 2
SMR	Small Modular Reactor
TRIAD	Thermal Reactor Integrated Analysis and Design
WIC	Weighted Isotopic Composition

Chapter 1: Introduction

Small Modular Reactors (SMRs) are designed to provide clean, consistent, and safe energy, positioning Canada to advance towards a low-carbon economy [1]. Historically, SMRs have been manufactured with an electrical power output up to 300 MW per module and shipped for installation to then power buildings. Royal Military College (RMC), located in Kingston, ON, houses the SLOWPOKE-2 (Safe LOW-Power Kritical Experiment) SMR. Primarily, it is used as a research micro-reactor with a recorded maximum thermal power of 20 kW.

This thesis addresses two main goals: first, the establishment of an accurate means of measuring the thermal power of the RMC SLOWPOKE-2 SMR, and second, the measurement and analysis of changes in fissile content before and after refuelling. The impact of these tasks will help create an enhanced fuel monitoring system at RMC based on neutron measurements at stand-off distances outside of the reactor core. Thus, this research would contribute to previous successful attempts at such stand-off monitoring, such as was originally demonstrated at the National Research Universal (NRU) reactor in Canada by researchers at Canadian Nuclear Laboratories (CNL) [2]. Each of the two items will include a review of previous approaches, followed by proposed methods for this work.

Further, as part of item two, this study on the SLOWPOKE-2 SMR investigates the practicality of utilizing the stand-off monitoring system on SMRs and, by extension, on other reactor types such as light-water reactors (LWRs) and pressurized heavy water (PHWs)

reactors. The ability to monitor SMR systems at stand-off distances would result in an increased effort to adhere to safeguards set by the International Atomic Energy Agency (IAEA) for nuclear non-proliferation.

1.1 SLOWPOKE Reactors

In 1985, the SLOWPOKE-2 SMR was installed at RMC as a self-regulating, low-power vessel-in-pool nuclear reactor intended for academic research on neutron production and professional development for the Department of National Defense and Canadian Armed Forces. The SLOWPOKE family of reactors are currently the only globally deployed brand of reactors, which are safe enough to be operated unattended. Altogether, [between 1976 – 1984], Atomic Energy of Canada Ltd. (AECL) supplied eight SLOWPOKE reactors to universities and research centers across Canada and Jamaica. Three of these eight reactors currently remain operational [3].

The original SLOWPOKE-1 reactor was explicitly designed so that an accurate heat balance could be performed with the reactor operating at an approximate power of 5 kW [4]. To make this possible, the reactor container was thermally insulated, and heat could be removed through a water coil located just above the reactor core. A simple heat balance approach determined the amount of reactor heat being removed via the cooling coil. The additional small fraction of heat lost by leakage through the insulated reactor container was calculated by applying Newton's Law of Cooling to the time decay of the water temperature in the reactor container. From this heat balance, an ionization chamber in a specific location

adjacent to the reactor was calibrated for absolute reactor power. Previously, during the commissioning of the SLOWPOKE-1 at Chalk River Laboratories (CRL), an Am: Be neutron source was located at the center of the reactor core when there was no fuel in the core, and the signal from the ionization chamber located in its same specific position was observed. Using the absolute power calibration of this ionization chamber, the "effective power" of the Am: Be source was defined as 0.0147 mW.

During the commissioning of SLOWPOKE-2 in Ottawa, the same Am: Be neutron source that was used for SLOWPOKE-1 was placed at the center of the reactor core (similarly with no fuel in the core), allowing for the calibration of the ionization chambers next to the reactor for absolute power. The accuracy of utilizing a constant "effective power" determined by a different reactor and applying it to the absolute power calibration of another similar reactor was assessed. Results indicated that this method could result in systematic errors in the absolute power calibration of around 25% [5].

The relationship between reactor power and thermal neutron flux was established using the absolute ionization chamber calibration and neutron activation measurements. Thus, it was determined for this SLOWPOKE-2 that the thermal neutron flux in a small (inner) irradiation site is $10^{12}\ n/cm^2s^1$ at a reactor power of 16 kW. The control system neutron flux detector channel would then be calibrated for this thermal neutron flux. Thus, the power output for the SLOWPOKE-2 SMR at RMC is controlled using a neutron flux setpoint.

1.2 Weighted Isotopic Composition

The refueling of the RMC SLOWPOKE-2 reactor in September 2021 was the first since the reactor began operation in 1985. By this time, the old core had undergone sufficient burnup, converting uranium into plutonium, which warranted replacement with a fresh uranium core. Of interest to this project is the change in weighted isotopic composition between the old and new reactor cores. The weighted isotopic composition is a weighted sum of fissile uranium and plutonium isotopes in the core composition, depending on each isotope's contribution to in-core neutron flux per unit thermal power [2]. One of the challenges this thesis addresses is quantifying the differences in weighted isotopic composition before and after refuelling, based on neutron flux and reactor thermal power measurements. Collaborators at CNL have estimated this difference to be approximately 2% and is to be confirmed by measurements [2].

1.3 SLOWPOKE-2 Geometry

SLOWPOKE-2 uses sintered uranium dioxide (UO_2) pellets arranged end to end with a diameter of 1 cm and a length of 20 cm. 20% of the fuel pellets are in the form of fissile Uranium-235, whereby the fuel would be considered low-enriched uranium (LEU) [6]. The core housing is made from zirconium alloy (Zircaloy-4) and currently contains 195 fuel pins (after the September 2021 refuelling). Beryllium is used as a reflector and is shaped into an annulus, a lower reflector and a top reflector shim intended to reflect neutrons back to the core. The reactor core uses semicircular beryllium shim plates, whose thickness is adjusted to compensate for fuel burnup and maintain the licensed reactivity of the SLOWPOKE-2. The cadmium

control rod is located at the center of the reactor vessel and is used to control the reactivity of the core by adjusting its position from fully inserted to fully withdrawn (20.32 cm above the bottom reflector). Cadmium is used for the absorption of thermal neutrons in the form of a control rod due to its high thermal neutron capture cross section, allowing it to regulate the neutron flux based on the location of the control rod within the core.

The reactor container, containing the core, is submerged in a cylindrical pool approximately 6 meters deep, filled with deionized light water that serves as both the moderator and coolant, as well as shielding. Temperature gradients within the pool create thermal stratification and induce free convection currents. These effects will be demonstrated through CFD simulations of the reactor pool and validated experimentally using a vertical array of eight thermocouples positioned at different heights. One of the main safety features of the SLOWPOKE-2 reactor is its negative temperature and void coefficients. A negative temperature coefficient means that when the temperature in the pool increases, its reactivity decreases, whereas a negative void coefficient indicates that any formation of voids or bubbles in the moderator (water) similarly leads to a decrease in reactivity, thereby enhancing the inherent safety of the system. Regarding reactivity, it is influenced by the temperature of the entire core, including the fuel and moderator, which is subsequently indicated by the temperature of the water within the container. In this case, the external pool water acts as a heat sink for both the reactor core and the container.

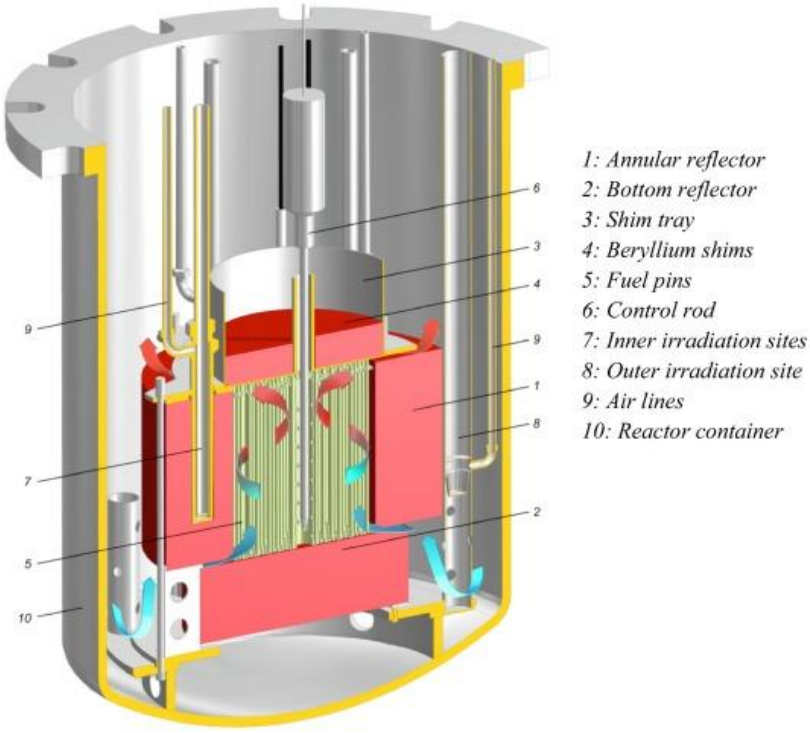

Figure 1: Reactor container components with deionized water inlet and outlet visualized throughout the reactor fuel pins (taken from Puig et al. (2016)) [7].

SLOWPOKE-2 has several sensors that are used to monitor the reactor. Temperature probes are located at the inlet and outlet gap where water can flow in and out to moderate and cool the core. There is also a neutron flux detector located near the fuel cage, as well as external neutron flux detectors (He-3 and B10+) above the reactor and in the control room, respectively. Internal detectors are recorded in real-time in reactor logs, which can all be controlled through a control software called the SLOWPOKE Integrated Reactor Control and Instrumentation System (SIRCIS), which uses LabVIEW to control parameters such as the control rod setpoint. The Helium-3 (He-3) Neutron counter detects thermal neutrons that provide an output pulse proportional to Q = 764 keV through the following reaction [8]:

$$He^3 + n\ (\text{thermal}) \rightarrow H^1 + H^3 + Q$$

The B10+ detector is a hybrid detector, utilizing both the He-3 detection process described above, as well as neutron capture by B-10. B-10 absorbs thermal or slow neutrons and generates alpha particles and lithium nuclei through the following reaction [9]:

$$B^{10} + n \rightarrow \begin{cases} Li^7\ (1.01\ \text{MeV}) + \alpha\ (1.78\ \text{MeV})\ 6\% \\ Li^7\ (0.84\ \text{MeV}) + \alpha\ (1.47\ \text{MeV})\ 94\% \end{cases}$$

Figure 2 displays the reactor control room interface and the operating parameters that can be adjusted, such as the inner site flux setpoint, which corresponds to a specific measured neutron flux used to set the reactor power. The display also showcases the relative position of the control rod in the reactor core and the inlet and outlet temperature.

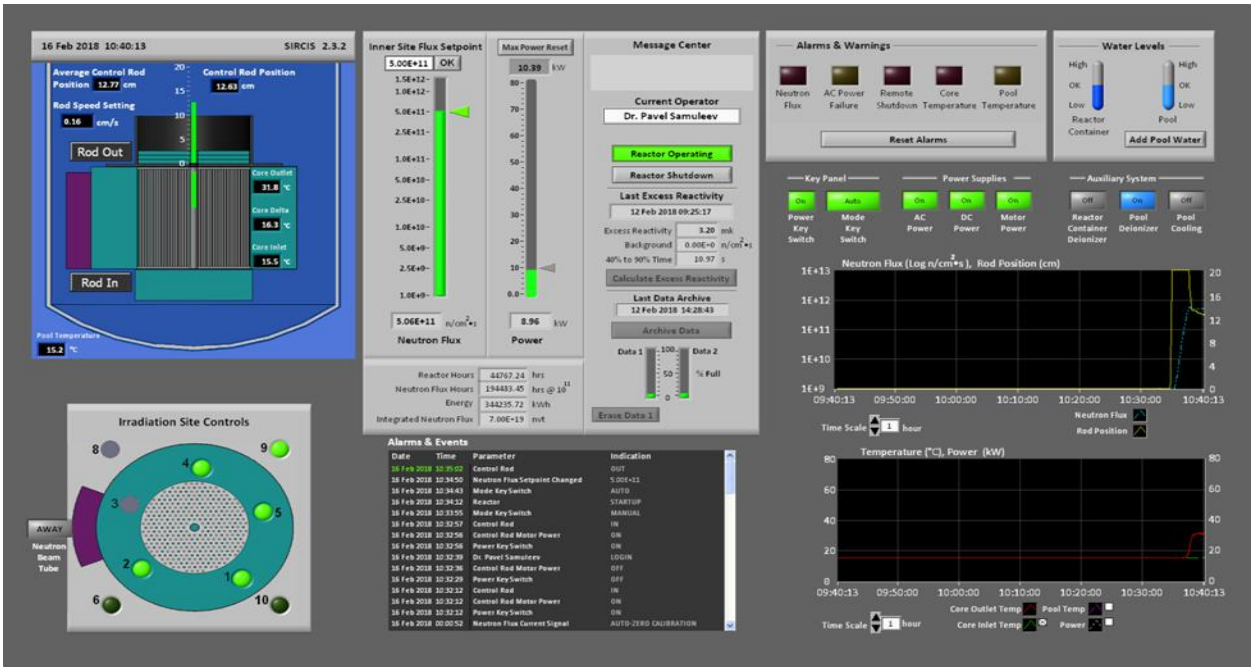

Figure 2: Reactor control room interface with custom neutron flux setpoint corresponding to a thermal reactor power (in kW). **(Top Left)** Control Rod relative position with a maximum displacement of 20.32 cm [8].

1.4 SLOWPOKE-2 (at RMC) Power Calibration

For the SLOWPOKE-2 SMR at RMC, a different radio isotopic neutron source called Ac-Be was used. Using the Ac-Be neutron source with a known "effective power" constant, one of the two neutron ionization chambers was calibrated for power. The full power level is based on a neutron source with a neutron flux of 10^{12} n/cm^{2}s and was determined to be 17.7 kW. Some of the issues that can be noted for this method include the assumption that the original heat balance results of the SLOWPOKE-1 reactor can be applied to the SLOWPOKE-2 reactor. In addition, different neutron sources with varying effective powers were utilized for each reactor calibration. These challenges and limitations highlight the need for a more accurate and reliable method for power calibration, as currently, they are, at best, $\pm$25% accurate [10]. The location of the control rod in the center of the fuel cage is adjusted to control

the reactivity, and the neutrons emitted are detected using He-3 and B10+ detectors. The control rod, a key component of the reactor's safety system, absorbs neutrons and thus controls the rate of the nuclear reaction, thereby regulating the reactor's power output.

Di Giovanni [10] conducted a comprehensive investigation into the RMC SLOWPOKE-2 core before and after the recent refuelling in September 2021. The new low-enriched uranium (LEU) core, manufactured at the Canadian Nuclear Laboratories (CNL), was a key focus of the study. Specifically, Di Giovanni [10] delved into the temperature differences between the two cores and estimated the energy difference between the old and the new core. A CFD model of the SLOWPOKE-2 nuclear reactor in ANSYS Fluent was meticulously constructed, providing a detailed estimation of its thermal power based on measurable operating parameters [11]. This work also explored the ability to monitor nuclear reactor power remotely [10], which would provide an additional safeguard against the proliferation of nuclear material.

Puig & Dennis also explored the possibilities for improving the performance of the LEU-fueled SLOWPOKE-2 reactor design concerning the fuel pins distribution throughout the core [12]. While both investigations attempt to focus on the design of the SLOWPOKE-2 core, this thesis concentrates on the heating distribution of the reactor pool, with the goal of correlating power based on the heating profile.

1.5 Motivation

Task 1 of this thesis involves establishing an accurate means for measuring the reactor thermal power. This task would be crucial in not only utilizing the standoff nuclear reactor monitoring system proposed by van der Ende et al. [2], but also in reevaluating the calibration of the SLOWPOKE-2 reactor through establishing a proper baseline after the installation of the new core with 195 pins instead of 198. Changes in the thermal power output of the SLOWPOKE-2 reactor could be correlated to the newer geometry with fewer fuel pins in the outer fuel cage and the different weighted isotopic composition of the core (estimated to be a difference of 1.95% by CNL [10]), and the relocation of the beryllium shims. Currently, the thermal power in the control room is calculated from the neutron flux (measured by neutron detector in units of thermal neutrons $cm^{-2}s^{-1}$), which is related to the thermal power (in kW) via a proportionality constant. This method for estimating the thermal power was proposed by Duchesne [5], where the proportionality constant depends on the flow rate and pressure loss from frictional forces in addition to the inlet and outlet temperature, which are more applicable to the old geometry. As a result of the aforementioned factors, there needs to be a newer method to measure the reactor thermal power of the SLOWPOKE-2 reactor after the refuelling that occurred in September 2021. Results from the previous thesis by Di Giovanni [10] highlighted the change in the temperature difference between the inlet and outlet from both cores with no change in the thermal power displayed in the reactor control room, showcasing the motivation of utilizing a CFD software to model the free thermal convection present in the reactor. The CFD model would, therefore, provide the temperature profile at the inlet and outlet, which would be

compared with inlet and outlet readings sampled using SIRCIS in the reactor control room. The temperature was then used to estimate the thermal power output. It is essential to note, however, that the exact location of the inlet thermocouple isn't precisely known, and the work performed by Di Giovanni [10] was intended in part to confirm the findings by CNL of the reactor power using ANSYS Fluent instead of STAR-CCM.

The Fluent model that most agreed with the converged model in STAR-CCM at CNL showcased significant discrepancies in the inlet and outlet temperatures (49.2 °C and 71.5 °C respectively in Fluent) at half power (8.85 kW) compared to the experimental readings (slightly above 25 °C for inlet and slightly above 40 °C for outlet) [10]. In addition to the unknown exact location of the outlet thermocouple, there has been significant uncertainty observed in the thermocouples that are placed near the inlet, outlet, and core, based on noise histograms that showcased the higher noise levels at the inlet, which affected the ΔT parameter [10]. The source of the noise is still unclear, so if any comparisons are made in the future, the outlet should be the primary baseline due to the lower noise levels. Thus, this introduces limitations for the comparison between CFD simulations of the expected thermal power from the reactor core, as it calculates the delta T between the inlet and outlet thermocouples. Consequently, if comparisons were to be made with the already existing setup, then it was noted by Di Giovanni [10] that lower power levels should be the primary focus to reduce the effect of the temperature probe noise, while noting the scarcity of the data at power levels other than half power.

As previously mentioned, completing task 1 of this thesis is essential in obtaining an accurate thermal power with a relatively insignificant error compared to previous trials, which will be utilized in the stand-off monitoring system of the neutron flux as proposed by van der Ende et al. [2]. The stand-off monitoring system would ultimately allow for a more efficient method of adhering to the current guidelines set by the IAEA, which require the loss of Pu, HEU, and U-233 in irradiated fuel to be detected in under 90 days [13]. This monitoring system could serve as a tool for the safeguarding of nuclear fuel, which would help ensure the peaceful use of nuclear materials. While SLOWPOKE-2 does contain low-enriched uranium (LEU), it also possesses plutonium (Pu) in its irradiated core, and the correlation between its neutron flux and power can be used to assess the feasibility of remotely monitoring the amount of fissile material in the core.

1.6 Objective

The objective of this thesis is to tackle the two motives mentioned previously: establishing a means of accurately measuring the RMC SLOWPOKE-2 reactor's thermal power and analyzing changes in fissile content before and after refuelling. The thermal power of the reactor core was experimentally and theoretically determined using a heating source with a known thermal power output, as well as through heat balance equations based on the temperature profile of the pool. An immersion heater is a heating source that can be submerged under water, and the temperature profile of the pool can be obtained using an array of thermocouples attached vertically to an aluminum rod. In order to use the immersion heater setup to calibrate the reactor power, a CFD model using ANSYS Fluent

will be implemented to assess the location of the immersion heater assembly that would resemble similar heating profiles to the reactor core across the water pool.

The immersion heaters in this work are mounted on an aluminum platform, machined at the Department of Physics, Engineering Physics & Astronomy Machine Shop in Stirling Hall. Once mounted on the aluminum assembly, electrical connections are configured between the immersion heaters, the junction box, and the outlets available in the reactor room. Since the reactor core flux is regulated based on the position of the cadmium control rod, the reactor nominal power can be set to different power levels. Three immersion heaters (two 1.5 kW and one 6 kW) are used to create five different power level steps (1.5 kW, 3 kW, 6 kW, 7.5 kW, and 9 kW) which are used to calibrate the reactor core power. The power output of the immersion heaters is measured using voltage and current probes attached to a power meter. Type-K thermocouples are attached to an aluminum rod that spans vertically across the reactor pool, providing real-time temperature data at eight different locations using a data logger connected to a computer.

Ultimately, this allows for the direct comparison of the thermal power output from a known heating source to the reactor core. The average immersion heater heating rate (dT/dt) in $°C/min$ across the 8 thermocouples is used to calibrate a constant that will compare the nominal reactor power. PicoLog 6 [14] is used as the data logging software for the thermocouples, and the data are exported to a CSV file, where a Python code filters the time range and handles the sampling intervals.

As previously mentioned, the second portion of the thesis involves analyzing the change in fissile content after the refuelling in September 2021 by assessing the enhanced fuel monitoring system that has already been tested at the NRU at Chalk River by van der Ende et al. The theory related to the enhanced monitoring system that was employed previously will be discussed in detail in Chapter 2: State-Of-Knowledge.

Chapter 2: State–of–Knowledge

2.1 Neutron Flux Data

The theory by van der Ende et al. suggests that the ratio of reactor power to detector count rate is a meaningful quantity to follow due to the clear linear dependence of the neutron detection count rate on the nuclear reactor power [2], as seen in Figure 3. This quantity establishes the motivation to remotely monitor the neutron flux of a nuclear reactor at stand-off distances, which is also related to the isotopic inventory since the ratio of the average neutron flux ($\langle\phi\rangle$) to the thermal power (P_{tot}) is sensitive to changes in the fissile isotope inventory, as seen in the following equation:

$$\frac{\langle\phi\rangle}{P_{tot}} = \left[N_A \sum_i \frac{m_i \langle\sigma_{f,i}\rangle E_{f,i}}{w_i}\right]^{-1} \quad (1)$$

where N_A is Avogadro's number, m_i and w_i are the mass [g] and atomic weight [g mol^{-1}] respectively for the i^{th} fissile isotope, E_f is the energy released per fission, and σ_f is the microscopic cross-section [cm^{-2}].

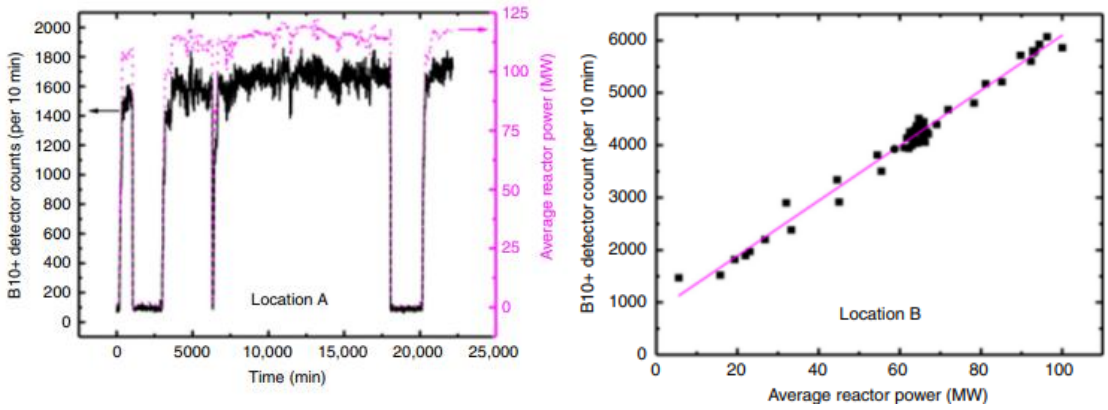

Figure 3: Neutron count rate at Location A (17m from reactor core) and Location B (69m from reactor core) of the National Research Universal (NRU) reactor in Chalk River, Ontario, Canada**. (b)** showcases the count rate (per 10 min) of the B10+ detector and the average thermal power (in MW) vs time (in min) during reactor start-up and shut-down periods at location A. **(d)** showcases the direct relationship between the neutron count rate (per 10 min) and average reactor power (in mW) at location B. Reproduced from Ref [2].

Uranium isotopes (U-235 and U-238) and Plutonium isotopes account for 99.9% of the fissile material in thermal fission reactors, where U-235 is naturally present as fresh fuel and other U and Pu isotopes exist via transmutation or online refuelling [2]. Consequently, the fissile Uranium and Plutonium mass inventory significantly changes during refuelling, which is why monitoring the neutron count rate/unit power for some cases of interest (before and after refuelling) to a base reference case can be related to the fissile content in the reactor, as exhibited by Equation (1). The fissile isotope mass inventory at the time of measurement also has to be estimated, possibly using simulations or already published findings from CNL, where current estimates show a 1.95% difference between both cores in the isotope inventory [10]. Equation (1) has been observed to be in good agreement with experimental observations at the National Research Universal (NRU), where it demonstrated the possibility of tracking and verifying changes in the total amount of fissile

content in the reactor's core [2]. This leads to the motivation to observe this relationship on SMRs like the SLOWPOKE-2 reactor.

Currently, there are two primary instruments for neutron flux detection in the SLOWPOKE-2 facility: the detector located in the reflector region of the core (displayed on the control room computer in units of thermal neutrons $cm^{-2}s^{-1}$), and He-3 and B10+ neutron flux detectors located on the ceiling above the reactor and in the reactor control room, respectively (in units of counts/600 s). The previous thesis by Di Giovanni [10] mainly analyzed the He-3 neutron detector on the ceiling and the internal flux detector. However, since the system in the reactor control room used to monitor the internal neutron flux works by operating the reactor at a specific neutron flux setpoint and adjusting the control rod movement to stay at said value, then there would be no noticeable difference between the old and new core, as noted in the previous thesis by Di Giovanni [10].

Task 2 of this thesis also involves the analysis of the relationship between the detector count and the thermal power and the correlation to the environment. The sensitivity analysis can be done by indicating the intervening shielding/building material between the detectors and the SLOWPOKE-2 reactor core, the effect of the environment where the detector is placed, and the changing operational environment. Using the B10+ and He-3 detectors, there would ideally be a one-to-one correspondence between the flux per unit power vs. the weighted isotope inventory, which would display the practicality of utilizing this method to monitor SMRs by creating a more efficient method of detecting the diversion of significant quantities of Pu, HEU, and U-233 in irradiated fuel in under 90 days. This can be done by normalizing the neutron count per thermal power (with background subtracted) and plotting

it against weighted isotopic composition before and after refuelling (see Figure 4). The weighted isotopic composition would be based on the fissile isotopic composition at the time of measurement, which can be determined through core-following calculations. Finally, the change in fissile content according to the proposed monitoring system would then be compared to the actual change in fissile content during refuelling, as illustrated by CNL. The changes in the fissile content can then be broken down into different isotopes, such as ^{235}U, ^{238}U, ^{239}Pu, and ^{241}Pu and monitored vs. time to monitor nuclear emanation at stand-off distances.

Another source of neutron count rate could be the ion chamber at the bottom of the reactor core, which detects different types of ionizing radiation, including gamma rays, but could theoretically only isolate neutrons. Previous calibrations have been attempted with an Am-Be source, but the background noise provided significant uncertainties that the power calibration process could only be $\pm 25\%$ accurate at the most favourable estimates [10].

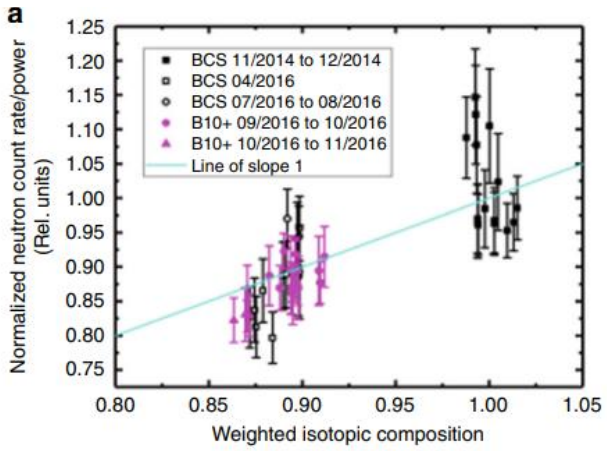

Figure 4: The normalized neutron count rate/power (relative to a standard case since there was no calibration) vs. weighted isotopic composition from TRAID simulations for the NRU. The linear fitting yields a slope of 1.08 ± 0.13 and an ordinate intercept of -0.08 ± 0.12, which agrees within standard deviation to the one-to-one correspondence predicted by the equation used to predict this behaviour [2].

2.2 Immersion Heaters

Three immersion heaters are used in this work for reactor power calibration, which is currently determined based on a neutron flux setpoint. Using two 1.5 kW immersion heaters and one 6 kW immersion heater, five power steps could be simulated with the heaters for power calibration. The five power levels were (1.5 kW, 3 kW, 6 kW, 7.5 kW, and 9 kW), where a junction box was constructed to switch between all three heaters selectively. The 6-kW heater is a 208V 3-phase Bucan screw plug immersion heater with a Watt density of 30 W/in^2 and a tube diameter of 0.43 in. Since long-term reliability and even heat distribution are more important, given the low conductivity of deionized water, a lower Watt density (30 W per square inch) would be more beneficial as compared to a higher Watt density heater. The configuration for the three-phase system is in a delta connection of three phases where

the line voltage is equal to the phase voltage (for phases X, Y, Z), but the phase current (I_P) and line current (I_L) are related by:

$$I_L = \sqrt{3}\, I_P$$

With the line current leading the phase current by 30 degrees. Consequently, the total power (P_{total}) drawn from the line is expressed by:

$$P_{total} = \sqrt{3}\, V_L I_P cos\,(\phi)$$

Here, V_L is the line Voltage (in V), and $\cos(\phi)$ is the Power Factor, which is typically unity for resistive loads such as heaters.

Using crimp connectors, the X, Y, and Z hot terminals were connected to a 10/3 AWG stranded wire cable. The voltage drops across the length of the cable to and from the immersion heaters have to be less than 5%. Based on the following calculation, 10 AWG copper cables were chosen with three hot conductors (Black, Red, and White) and a ground (Green):

$$\Delta V = I\,R = \frac{6000\ W}{208\ V} * \left(0.00335 \frac{\Omega}{m} \times (2 \times 30) m\right) = 6.97\ V \text{ or } 3.34\% \text{ of } 208\ V$$

As for the two 1.5 kW immersion heaters, Grainger single phase screw plug immersion heaters rated for 120 V AC with a heating density of 23 W/in^2 were selected to ultimately test 5 power steps in conjunction with the 6 kW heater. Both 1.5 kW heaters included hot, neutral, and ground screw terminals where solid 12/2 AWG solid core copper wire can be wrapped counterclockwise for electrical connection. Similarly, the voltage drop across the

entire length of cable used from the outlets to the immersion heaters was calculated to ensure a voltage drop of less than 5%

$$\Delta V = I\,R = \frac{2000\ \text{W}}{120\ \text{V}} * \left(0.00531\frac{\Omega}{\text{m}} * (2 * 30)\text{m}\right) = 5.31\ \text{V or } 4.4\%\text{ of } 120\ \text{V}$$

The cable grade for both single and three-phase heaters was SOOW (Service cord Oil-resistant jacket, Oil-resistant insulation, Weather- and Water-resistant), as the cables must be submerged in the deionized water pool towards the immersion heater plate. SOOW cables are compliant with NEC (National Electric Code) standards and are rated for 600 V. They are also durable and flexible due to their rubber insulation and jacket which would be resistant to mechanical stress, bending, and flexing. SOOW cables can withstand a broad range of temperatures ($-40°C$ to $90\ °C$) making them suitable for the reactor pool [15]. During electrical installation, the outer jacket covering all four wires for the 10/3 solid copper cable was stripped at the ends to expose each conductor with its insulation that was stripped such that the copper wires could be connected to the screw terminals on the switch using crimp connectors.

Selectively switching which immersion heaters were on was vital for obtaining five power steps using all three immersion heaters. A junction box was designed to house three switches, one for each of the three immersion heaters, each with their own switch plate. Three immersion heaters were chosen for this experiment based on budget and the availability of electrical outlets with their own separate breakers in the reactor hall. One of the outlets was a Leviton L18-30P, which was rated for 30 A and 120/208 V (single or three-phase) but was located just outside the reactor room, which required 23 m of 10/3 AWG

SOOW cable that needed to adhere to a voltage drop of less than 5%. The other two outlets were located in the reactor room with their own separate breakers and were rated for 15 A and 120 V each. Appropriate locking plugs were used such that the cables would run from the switch boxes to the locking plugs to be connected to their respective outlets on one side and toward the immersion heaters on the other side.

The three-phase heater (6 kW) utilized a Leviton MS303-DSS 30 A, 600 V, three-pole switch that was non-grounding, which required a metal switch box for proper grounding, while two Leviton 15 A, 120/277 V DPST (Double Pole Single Throw) switches were used for the single phase 1.5 kW heaters. Both switches had a line side (towards the outlets) and a load side (towards the heaters). Leviton locking plugs rated for (30 A & 125/250 V) and (15 A & 125 V) were used for the three-phase and single-phase heaters, respectively (see Figure 5).

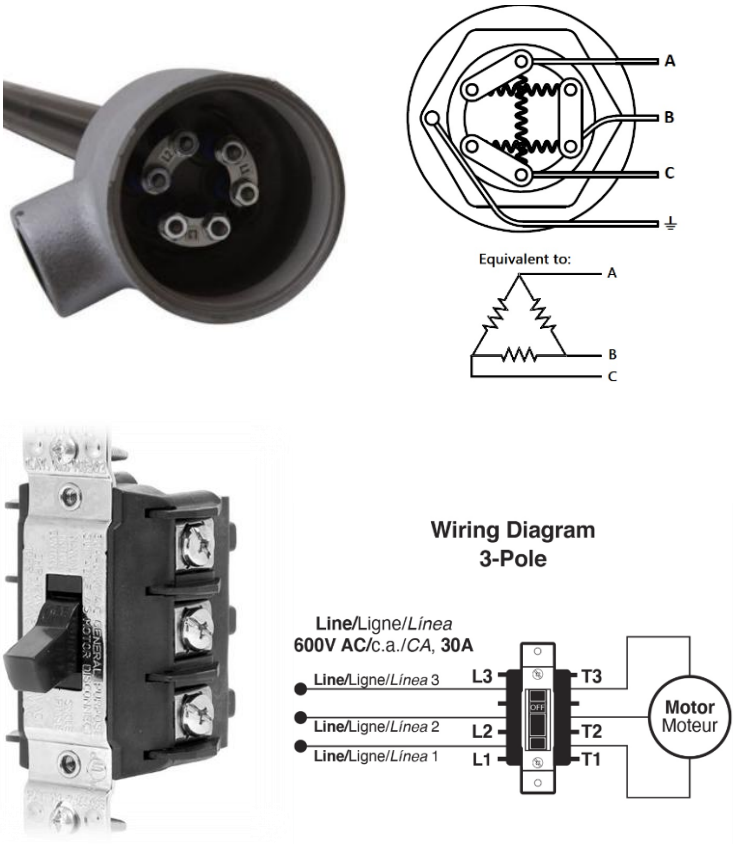

Figure 5: (Top Left) 6 kW immersion heater terminals with L1 / L2 / L3. (**Top Right**) Wiring diagram in delta configuration with A, B, and C hot phases with the ground screw terminal on the platform. (**Bottom Left**) The three-pole motor switch selectively turns the 6-kW immersion heater on and off depending on the desired power level. (**Bottom Right**) wiring diagram with line side towards outlet and load side towards immersion heaters [16].

Prior to being installed in the reactor pool, all three immersion heaters were tested in a 50-gallon water barrel to burn off any antioxidant coatings and to ensure proper electrical wiring. The two 1.5 kW immersion heaters were tested in the Stirling Hall student workshop as there were two 15 A / 120 V outlets with their own breakers, but the three-phase 6-kW heater had to be tested at the SLOWPOKE-2 facility since it was designed for the outlet present there. An aluminum plate was used to suspend all three immersion heaters, along

with proper fittings for the threaded base. As for the preliminary test using the water barrel, the aluminum plate was used with a wooden platform beneath as the rain barrel was wider than the plate (see Figure 6 and Figure 7).

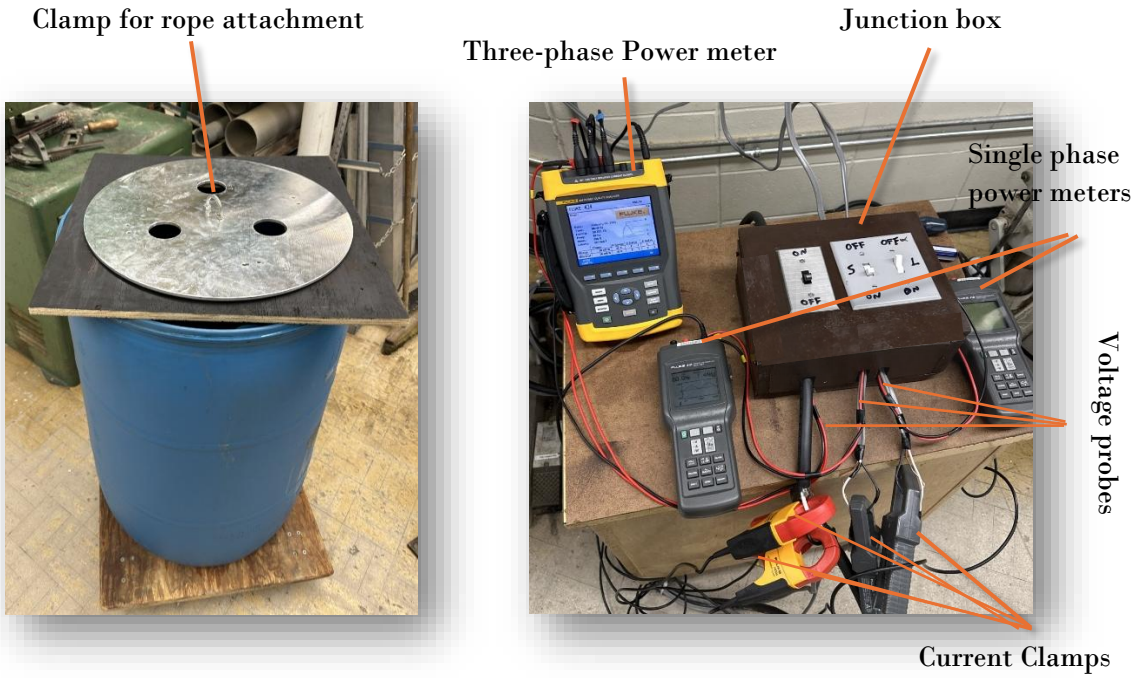

Figure 6: (Left) The top aluminum plate is placed using a wooden base so that the immersion heaters can be submerged while keeping the electronic connections out of the ionized water. (**right**) Two double-pole single-throw (DPST) switches for the 1.5 kW immersion heaters (in white) and one three-pole switch for the 6 kW immersion heater (in black). The voltage probes (L & N for 1.5 kW heaters and X, Y, Z for 6 kW heater) and current clamps around the hot terminals facing the direction from the junction box to the immersion heaters.

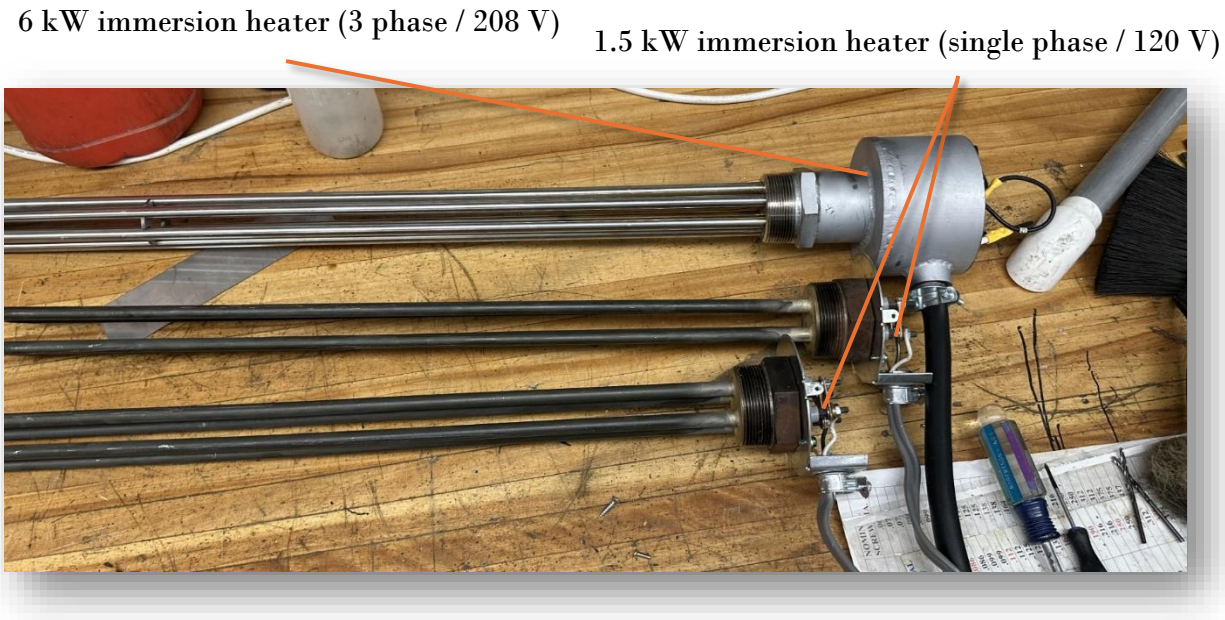

Figure 7: The three immersion heater coils have a 2" NPT threaded fitting that uses 2" nuts to stabilize the aluminum plates.

A thermal camera was used to investigate the temperature gradient in the barrel when the 1.5 kW immersion heaters were turned on. Figure 8 displays the thermal stratification after being turned on for ~ 40 minutes. It is interesting to note that the water in the stratified layer below the immersion heater coils was stable at $24 \pm 1°C$ while the water heated above to around 30.9 ± 0.5. This phenomenon will also be examined within the reactor pool using the thermocouple array, where one thermocouple is positioned below both the reactor core and the immersion heaters.

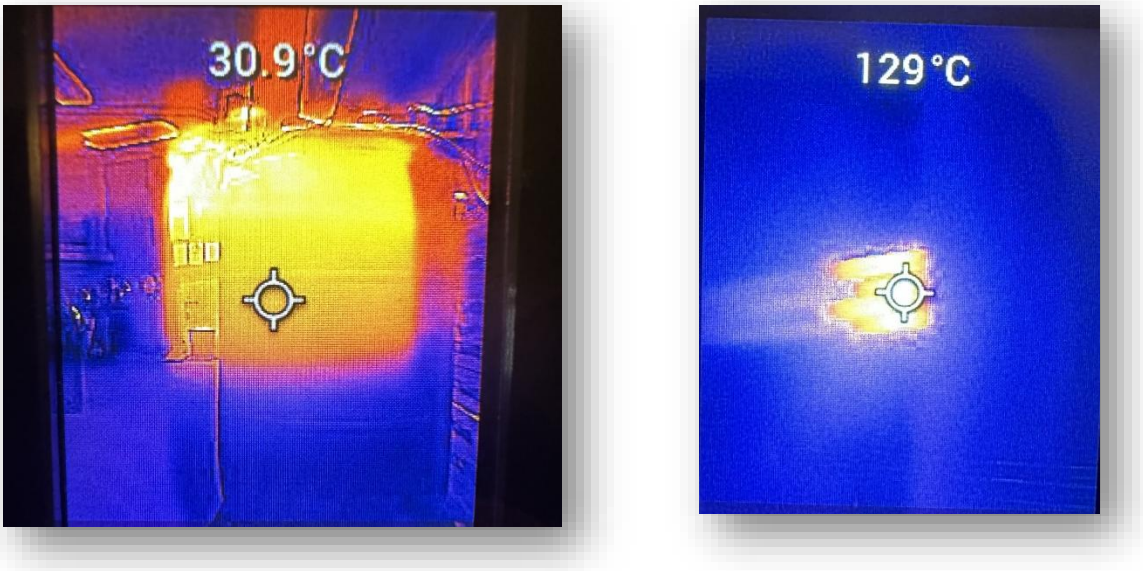

Figure 8: (Left) Thermal camera temperature gradient of the water with the thermal stratification beneath the heater coils. (right) the temperature of the coils above the water surface after 40 minutes.

2.3 Electrical Wiring

The single-phase immersion heaters included hot, neutral, and ground screw terminals, while the three-phase heaters included three hot (X, Y, Z) terminals and one ground. Two 120 V / 15 A single-phase outlets with their own breakers were used for the 1.5 kW heaters consisting of 11 m and 10 m of 12/2 AWG solid copper cable, and one 208 V / 30 A three-phase outlet with its own breaker was used for the 6-kW heater with 23 m of 10/3 AWG stranded copper cable. The junction box included two double pole single throw (DPST) switches and a three-phase switch.

Starting from the outlets, the outer jacket insulation for the ends of the 10/3 AWG and 12/2 AWG cables was stripped to expose the X, Y, Z, and G conductors and the black (hot), white (neutral), and solid copper conductors, respectively. The insulation for each

conductor was then stripped according to installation specifications for each locking plug. All three locking plugs had screw terminals where solid copper wires were wrapped counterclockwise around their respective terminals (black for hot/white for neutral/bare copper for ground), and stranded copper wires were twisted (black for X, red for Y, white for Z, green for ground). Towards the junction box, each switch housed in the junction box had either 12/2 AWG or 10/3 AWG wires going to and from the line side (towards the outlet) and load side (towards immersion heaters).

The connections on the switch boxes were screw terminals where copper wires for the single-phase system were also wrapped counterclockwise, but the stranded wires for the three-phase system were connected to the screw terminals using crimp connectors. Proper grounding was essential for the immersion heater setup. Therefore, grounded switch boxes were employed, as neither the 1.5 kW nor the 6 kW switches featured grounded screw terminals. Lastly, the 12/2 AWG and 10/3 AWG cables were then run from the junction box towards the immersion heaters, where screw terminals were used for electrical connections on the 1.5 kW heaters and crimp connectors were used to connect each phase from the 10/3 AWG cable to their respective stranded terminals on the 6-kW heater using crimp connectors. The circuit diagram with electrical connections for the two 1.5 kW and 6 kW immersion heaters can be seen in Figure 9.

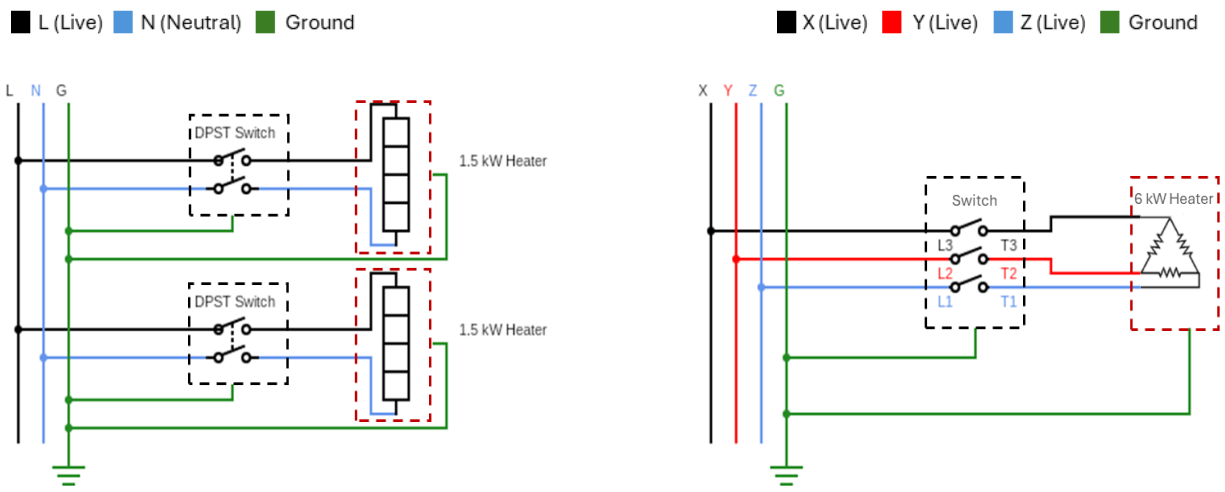

Figure 9: Circuit schematic for the **(Left)** Two 1.5 kW immersion heaters with DPST switches and **(Right)** 6 kW immersion heater in delta configuration with the three-phase motor switch. Note: In the text, 'white' refers to 'blue' as neutral in this figure for both single- and three-phase heaters.

The two single-phase power meters and the three-phase power meter required voltage and current readings. On the junction box, voltage probes were also connected to hot and neutral terminals for the single and three-phase heaters to monitor the line voltages. Current was measured using current clamps facing the direction of current flowing from the junction box towards the immersion heaters, where the outer jackets of the 12/2 AWG and 10/3 AWG cables were removed to expose the insulated black (hot) wire and black (X), red (Y), and white (Z) hot phases respectively (see Figure 10).

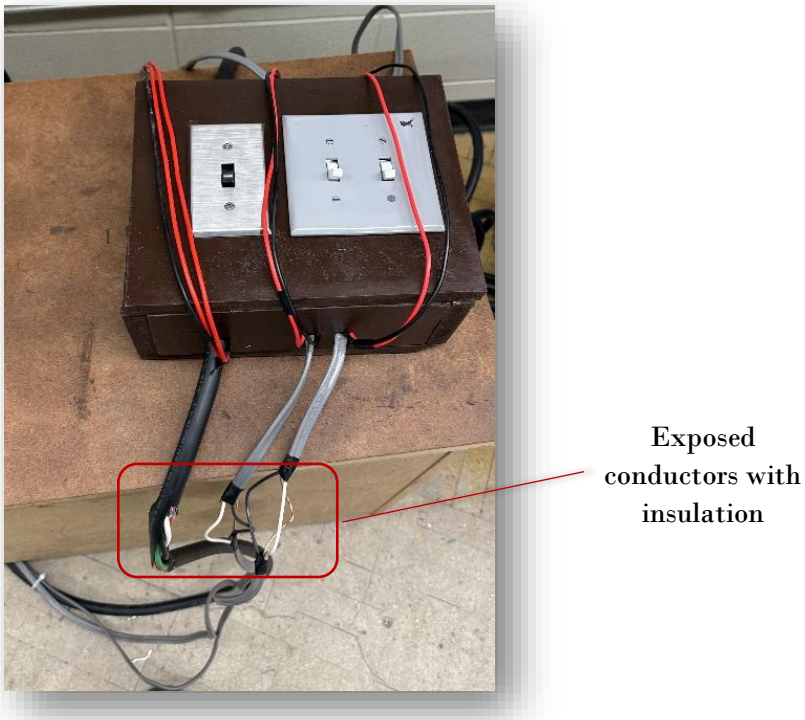

Figure 10: Exposed conductor insulation for the two DPST switches on the right and the three-pole switch on the left.

The continuity setting on a multimeter was used to assess the connections on the switches from the outlets (line side) to the immersion heaters (load side). Additionally, the same probe was used to ensure that the DPST and three-phase switches were always properly grounded.

2.4 Aluminium Assembly

The aluminum assembly used to suspend the immersion heaters in the reactor pool was assembled from T6 grade 6061 aluminum. Four 2″ x 3″ thick hollow tubes with a length of 6 ft were used for the legs, and brackets were manufactured from additional tubing. T6 aluminum was chosen since aluminum has low neutron absorption and is easily machined due

to its increased hardness from quenching and artificial aging [17]. A band saw machine was used to cut 2″ long sections from the legs, and then those sections were cut in half to give two brackets. The brackets were used to connect the plate holding the immersion heaters to the legs and a ring on the bottom of the legs to stabilize the assembly. A milling machine was used to tap the brackets, and all the edges were sanded and filed down to keep impurities from entering the reactor pool (see Figure 11).

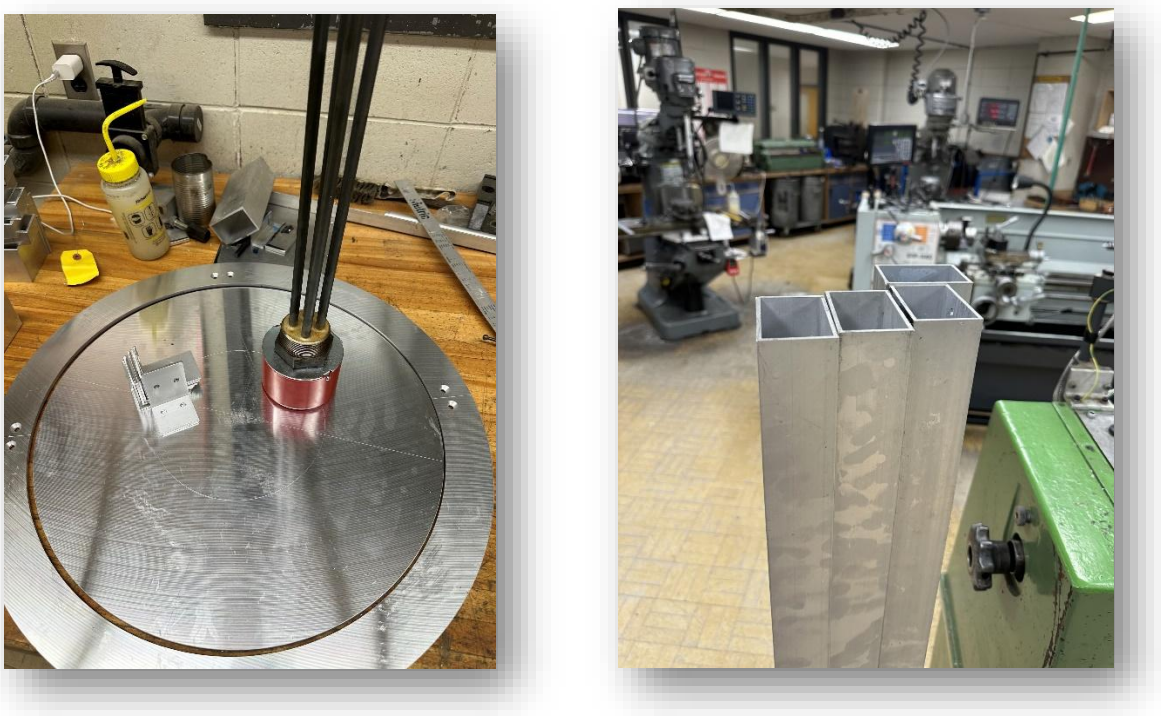

Figure 11: (Left) 22″ Aluminium top plate with 2″ width ring cut with milled brackets. (Right) 2″ x 3″ aluminum legs were used to stabilize the immersion heater assembly

The aluminum plate has a 24″ diameter and is 7000 series aluminum with ¼″ inch thickness and a high yield strength of 15,000 psi. 2″ on the outside was cut and used for extra stability at the bottom of the pool. As previously mentioned, the aluminum plate was placed

on top of a 50–gallon water barrel so that the electrical connections for the immersion heaters and the junction box could be properly tested before installation in the reactor pool. For consistency in the heating profile of the immersion heaters in comparison with reactor fuel heating on the reactor pool, the distance of the lower part of the immersion heater coils from the bottom of the reactor pool was designed to be 27 cm. All three immersion heaters would be placed on the circumference of a 22 cm diameter circle, similar to the diameter of the fuel core cage, and the diameter of the top aluminum plate has the same diameter as the reactor container (see Figure 12). Located at the center of the aluminum plate was a stainless-steel eye bolt that would be used with a pulley system above the reactor pool to lower the apparatus and adjust the location using the rope. The exact location of the aluminum assembly will be discussed in detail in Section: 3.2 Thermocouple array setup (see Figure 13).

Figure 12: (Left) The aluminum assembly is stabilized with the bottom 2" wide ring and no immersion heater. (Right) Immersion heaters are attached to the top plate and held in place using 2" nuts at RMC.

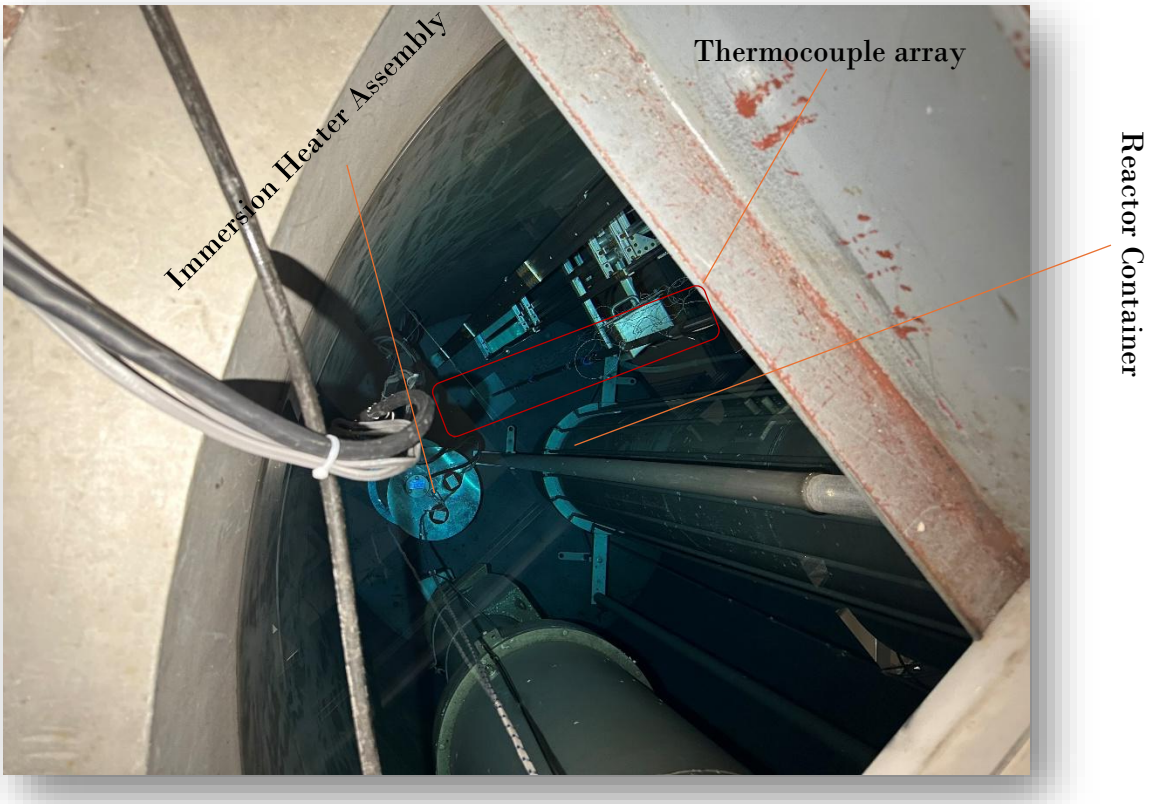

Figure 13: Top-down view of the lower right quarter of the pool that can be accessed. The immersion heaters are suspended on the aluminum plate, and the assembly was lowered using a pulley system attached to the clamp on the plate.

2.4 CFD Theory

Simulations performed by ANSYS Fluent model the hydrodynamics using the Navier-Stokes equations, specifically the mass continuity equation and momentum conservation equation in its finite volume form, where mass is neither added nor gained in a closed system [18]. For laminar flows involving heat transfer with inertial (non-accelerating) reference frames, the equations for mass (in Cartesian form for example) and momentum are respectively:

$$\frac{\partial \rho}{\partial t} = -\left(\frac{\partial(\rho u_x)}{\partial x} + \frac{\partial(\rho u_y)}{\partial y} + \frac{\partial(\rho u_z)}{\partial z}\right) \tag{2}$$

$$\frac{\partial}{\partial t}(\rho\bar{v}) + \nabla\,(\rho\,\bar{v}\,\bar{v}) = -\nabla p + \nabla\left(\bar{\bar{\tau}}\right) + \rho\bar{g} + \bar{F} \tag{3}$$

where ρ is the density, u is the axial velocity, p is the static pressure, $\bar{\bar{\tau}}$ is the stress tensor, and $\rho\bar{g}$ and $\bar{F}$ are the gravitational body force and external body forces that arise from interaction with the dispersed phase. For convective heat transfer, ANSYS contains an option to include an energy equation:

$$\frac{\partial}{\partial t}(\rho E) + \nabla\left(\bar{v}\,(pE + p)\right) = \nabla\left((k_{eff}\nabla T - \sum_j h_j \overline{J_j} + \left(\bar{\bar{\tau}}_{eff}\,\bar{v}\right)\right) + S_h \tag{4}$$

where k_{eff} is the effective conductivity, $\overline{J_j}$ is the diffusion flux of species j and S_h includes the energy from the heat of chemical reactions and any other heat source defined. The three terms in the sum are energy transfer contributions from conduction, species diffusion, and viscous dissipation.

The Boussinesq model was used as solutions converge faster for natural convection flows in steady-state form, and the temperature differences are not large ($\Delta T \approx 0.1\ ^{\circ}C$ magnitudes in our case) [19]. The density in this model will be treated as (only valid when $\beta(T - T_0) \ll 1$):

$$(\rho - \rho_0)g \approx \rho_0 \beta_T (\mathrm{T} - \mathrm{T}_0)g \tag{5}$$

Or

$$\rho = \rho_0\big(1 - \beta_T(T - T_0)\big) \tag{6}$$

where ρ_0, β_T, and T_0 are the constant density, thermal expansion coefficient, and the operating temperature, respectively. Fluids in these models have certain Reynolds numbers that distinguish which type of flow these simulations should consider. The Reynolds number is a dimensionless quantity where, at low values (when Re<2000), flows tend to be more dominated by laminar flow rather than turbulent flow [20]. This number is given by:

$$Re = \frac{\rho V D}{\mu} \tag{7}$$

where ρ is the density, V is the velocity, D is the inside diameter of our neck, and μ is the dynamic viscosity.

2.5 Theoretical grounds for power estimation

The estimation of power added to the pool is based on a comprehensive heat balance approach that accounts for heat input due to temperature increase, as well as heat losses via

convection, conduction, and evaporation by approaching the pool in a 'lumped' fashion. One of the assumptions this method relies on is subdividing the reactor pool into different vertical slices, based on the location of the thermocouples. A total of eight thermocouples were used to gather temperature data inside the pool at various depths over the same time interval. The rise in these temperature readings corresponded to a heating rate related to the power added and power lost from the pool. Two primary sources of losses were considered in the power calculation: losses from the top of the pool (via natural convection and evaporation) and losses from the bottom and sides of the pool (via conduction: see Figure 14). The water in the pool is surrounded by a 0.0096m stainless steel liner encompassing concrete embedded in dirt. This would constitute a series of thermal resistors that need to be accounted for: water to liner, conduction across the liner, liner to concrete, conduction across the concrete, concrete to soil, and then conduction through the dirt(see Figure 15).

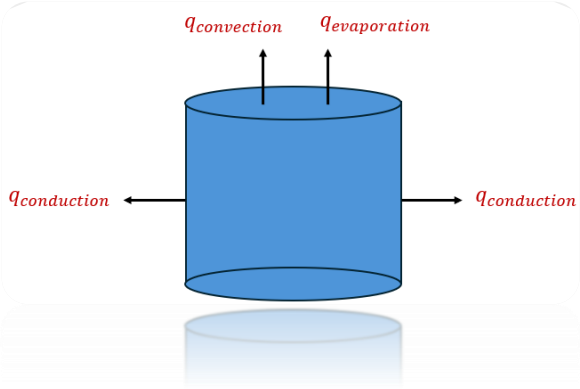

Figure 14 Sources of losses considered with the uncertainty estimate where only the shallowest volumetric slice had convection and evaporation losses

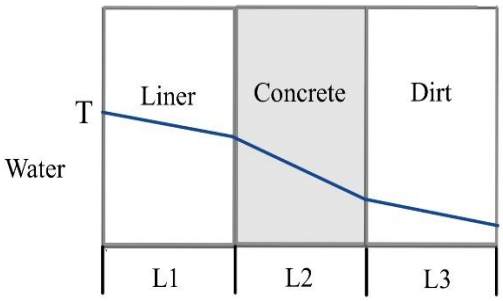

Figure 15 Conduction losses from bottom and side walls through (A) Stainless-steel Liner (B) Concrete (C) Dirt

Python was used to calculate the power added to and lost from each slice based on its location in the pool. The Python script assigns a depth to each thermocouple based on the channel number, and then, based on the depth and the height of the slice, a function calculates the volume depending on the height and the location in the pool. All eight slices have conduction losses through the reactor's walls, but only the topmost slice has convection and evaporation losses. Thus, the function for losses also depends on the depth of the slice and the temperature at every iteration for conduction losses. Using the losses and the mean heating rate, the power added to the pool can be estimated for different power levels. Currently, the SLOWPOKE-2 control room captures the inlet and outlet temperatures of the reactor core once every second while the reactor is turned on. The estimated power levels can then be

correlated with the change in inlet and outlet temperature and can be compared to current efforts of evaluating the power for the SLOWPOKE-2 [21].

$$q_{net} = \iiint \rho \, c_p \frac{dT}{dt} dt \, dV + q_{convection} + q_{conduction} + q_{evaporation} \tag{8}$$

$$\frac{dq_{added}}{dt} = \rho c_p \frac{dT}{dt} dV \tag{9}$$

$$q_{convection} = h \, A \, (T_w - T_{\infty 1}) \tag{10}$$

$$q_{conduction} = \frac{\Sigma k A (T_w - T_{\infty 2})}{L} \tag{11}$$

$$q_{evaporation} = (25 + 19v) \, A \, (X_s - X) \tag{12}$$

where ρ is the density of the water, c_p is the specific heat capacity of the water, q is the heat loss (in W), h is the convective heat transfer coefficient in $\mathrm{W\,m^{-2}(C°)^{-1}}$, A is the surface area, T_w is the water temperature in C° ,$T_{\infty 1}$ is the ambient air temperature in C°, k is the thermal conductivity in $W\ \mathrm{m^{-1}(C°)^{-1}}$, $T_{\infty 2}$ is the dirt temperature in C°, v is the velocity of the water at the surface in m/s, X_s is the maximum humidity ratio of saturated air, and X is the humidity ratio of the air where the evaporation is set to 0.01 [22]. The values of the constants used in the Python script for the theoretical heat balance power estimates are displayed in Table 1.

Uncertainty propagation follows standard error analysis, where uncertainties from heating rate measurements and volume estimation are combined. The uncertainty in net power is given by:

$$\sigma_{q_{net}} = \sqrt{\sigma_{q_{added}}^2 + \sigma_{q_{convection}}^2 + \sigma_{q_{conduction}}^2 + \sigma_{q_{evaporation}}^2} \tag{13}$$

where each term is propagated based on the measured and assumed uncertainties in the respective parameters.

Table 1: A list of all the constants used in the Python script for theoretical heat-balance power estimates. The constants are used for the heating rate calculation and the three sources of losses (convection, conduction, and evaporation)

Symbol	Value	Description
r_{water}	1.25 m	Radius of the water pool
$r_{aluminium}$	0.425 m	Radius of the aluminum fuel cylinder
c_p	4184 $J/kg\ K$	Specific heat capacity of water
ρ	998 kg/m^3	Density of water
h	10 W/m^{2}K	Convection coefficient for air-water interface
h_{dirt}	5 W/m^{2}K	Convection coefficient for dirt surface
k_{SS}	16 W/mK	Thermal conductivity of stainless-steel liner
$k_{concrete}$	1.75 W/mK	Thermal conductivity of concrete
k_{dirt}	0.5 W/mK	Thermal conductivity of dirt
L_{liner}	0.05 m	Thickness of stainless-steel liner
$L_{concrete}$	0.6 m	Thickness of concrete wall
L_{dirt}	1.0 m	Thickness of surrounding dirt
v	0.5 m/s	Estimated water velocity at surface
X_s	0.02	Humidity ratio of saturated air
X	0.01	Humidity ratio of ambient air

This methodology provides a robust estimation of power added to the pool while accounting for relevant heat losses. The assumptions made for thermal and convective properties ensure that the results remain within a reasonable range, and the uncertainty analysis provides confidence in the reported values.

Chapter 3: Methods

Regarding the first task of establishing a means of accurately estimating the thermal power output of the SLOWPOKE-2 SMR using the immersion heater apparatus with the thermocouple array, it was crucial to develop a setup of the apparatus that would mimic the heating profile of the reactor core. The location of the apparatus with respect to the core and the height of the aluminum plate that would suspend the immersion heaters was assessed using a CFD simulation of the heating profile from the reactor core and the immersion heaters. In addition to the position of the aluminum assembly and thermocouple array, the time needed to sample the data using the immersion heaters and the reactor core was calculated using a theoretical curve fit of the average heating profile from one of the thermocouple channels at 50% and 100% nominal reactor core power. The time constant was calculated at $\tau = 42$ min so the total time for measurement needed to be at least four time constants (~ 3 hours) and more if possible.

The schedule for measurements spanned two weeks, where the first week was comprised mostly of having the reactor core turned off fully with the chillers off (external coolers that would normalize the temperature of the pool to an average of around 15 °C) as well as the de-ioniser, which would otherwise force convection in the water. Thus, for consistency, the measurement campaign did not include either system turned on for most measurement days (aside from 6.11 kW using the immersion heaters). Ultimately, the

immersion heaters would be turned on selectively, and the corresponding power reading from the power meters would be used to match the reactor's nominal power. Table 2 summarizes the total time taken for measurements and the source of power in the reactor pool:

Table 2: Measurement campaign with multiple power levels using immersion heaters (measured) and reactor core nominal power (calculated from neutron flux in SIRCIS). The data sets with the chillers turned off overnight refer to the status of the chillers the day before measurements. Usually, the chillers and deionizing system would both be turned on overnight, but in some cases, either/both were turned off to account for the background heating for heat loss estimates.

Date	Reactor Core N. Power (kW)	Immersion Heater Power (kW)	Sample time	Notes
Jan 17th 2025	-	8.95	4 hours	Chillers turned on overnight.
Feb 24th 2025	-	7.33	5 hours	Chillers turned on overnight.
Feb 25th 2025	-	1.45	2 hours	Chillers turned on overnight.
Feb 25th 2025	-	2.90	2.5 hours	Chillers turned on overnight.
Feb 26th 2025	7.33	-	3 hours	Chillers turned on overnight.
Feb 27th 2025	-	6.11	4 Hours	Chillers turned on overnight
Feb 28th 2025	6.11	-	5 Hours	Chillers turned off overnight.
Mar 3rd 2025	8.85	-	5 Hours	Chillers turned on overnight.
Mar 4th 2025	2.90	-	6 hours	Chillers turned on overnight.
Mar 5th 2025	1.45	-	6 hours	Chillers and de-ionizer were turned off overnight.

Using the thermocouple readings from all eight channels, a Python code was developed to theoretically estimate the thermal power output solely based on heat balance equations between the thermal energy added from the reactor core and losses (convection,

conduction, and radiation). The results were solely used as an estimate of the power range expected from the heating profile of each thermocouple at the five power levels: 1.45 kW, 2.90 kW, 6.11 kW, 7.33 kW, and 8.85 kW.

The work conducted in this case study can then be divided into the following steps:

1) Take temperature measurements for 30 mins at 1s time steps at 50% and 100% SLOWPOKE-2 reactor core nominal power levels.
2) Build an ANSYS Fluent CFD model of the reactor pool with no immersion heaters to compare the vertical temperature profile at the known thermocouple location from Step (1).
3) Build an ANSYS Fluent CFD model assessing which location (further or closer to reactor walls) would be more comparable with the reactor core heating profile.
4) Use results from the CFD model to finalize the immersion heater aluminum assembly location in the pool.
5) Collect temperature measurements for at least 2 hours every 10 seconds at five power steps (1.45 kW, 2.90 kW, 6.11 kW, 7.33 kW, and 8.85 kW) using either immersion heaters or reactor core nominal power.
6) Estimate the theoretical SLOWPOKE-2 power based on the temperature profile of each channel (CH1 – CH8), resulting in a range of expected power output.
7) Calibrate and compare the thermal profile of the immersion heaters to that of the reactor core.

3.1 Data Acquisition

The data collected from the TC-08 Data logger from the thermocouples and the single and three-phase power analyzers were analyzed using Python. Preliminary estimates of the expected power range from the heating profile of each thermocouple using three reactor core power settings were estimated in March 2024 – April 2024. As for the immersion heaters, the data was collected from January 2025 – March 2025. Seeing as the reactor refuelling occurred in September 2021, in order to assess the changes in fissile content, it was necessary to attempt to match the nominal power and timeframe using the available data taken before refuelling. It is also important to note that the pool temperature at the start of the day is affected by the consecutive amount of times the reactor has been turned on during the week, so it was critical to ensure that the environments for power output comparisons (7.5 kW on immersion heaters and 7.5 kW from reactor core for example) were similar.

As previously mentioned, a TC-08 data logger was used to collect temperature and time readings in the form of a CSV file. To decrease the size of each file, temperature readings were sampled every 10 seconds, and the Python script would organize the data for analysis. A Fluke 437-II 3-phase power quality and energy analyzer was used to monitor the voltage, current, and, consequently, power output from the 6-kW immersion heater as it logs the readings every second and ultimately stores the data in its memory. The data is exported using an optical cable in the form of a CSV folder, and the average power is calculated as the immersion heater power for that run. Two other power meters were also used to monitor the power from the two 1.5 kW immersion heaters, and the data had to be recorded manually as

there was no available software compatible with the more recent operating systems, and the variation in readings was noted whenever either or both were used. Additionally, the SLOWPOKE-2 SIRCIS data collection system also records inlet, outlet, and pool temperature in addition to the internal neutron flux data. There are 86,400 data points each day as it records all four variables every second. Di Giovanni [10] noted the issues of the SIRCIS system where the neutron flux sample time is not always consistent with the thermocouple measurements as SIRCIS stops recording the neutron flux whenever the flux drops below a certain value, resulting in issues with combining both data sets. SIRCIS is written in LabVIEW, and the data is exported in CSV format for analysis using Excel and Python.

A Pico TC-08 data logger [23] was used to export the data at each timestep into a comma-separated value (CSV) file using PicoLog 6, which includes real-time data collection and display (see Figure 16 and Figure 17) [23][24]. The CSV file would be exported to a Python script, which would compare the temperature profile to a CFD simulation of the reactor pool. Both the heat-balance and heat rate (dT/dt) calibration approach for estimating the thermal power would utilize the CSVs exported from PicoLog 6.

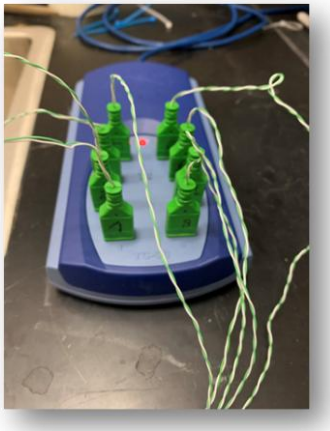

Figure 16: Pico TC-08 data logger connected to 8 type-K thermocouples

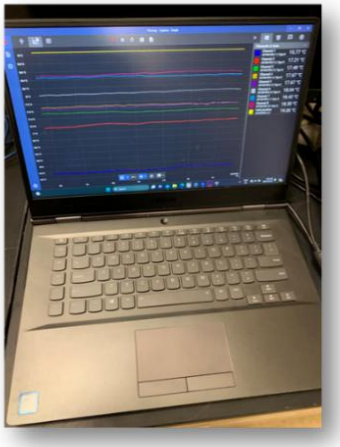

Figure 17: TC-08 Data logger connected to a laptop that uses PicoLog 6 to export eight temperature profiles

3.2 Thermocouple array setup

The SLOWPOKE-2 SMR was built in a concrete pool with an enclosed stainless-steel liner from the bottom and sides with a diameter, length and thickness of 2.46 m, 5.87 m, and 9.5 mm, respectively. Located inside the pool is an aluminum containment vessel that encompasses the fuel core with a total length of 5.27 m, 4.90 m of which is located beneath the water surface with an outer diameter of 0.61 m and a thickness of 9.53 mm. Using aluminum tape, an array of eight exposed-tip and polytetrafluoroethylene-insulated type-K thermocouples were attached to an adjustable telescopic pole with a maximum height of 7.4 m as seen in Figure 18 and Figure 19.

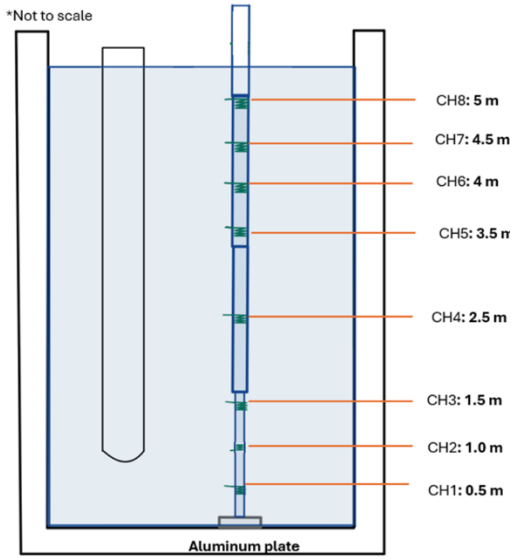

Figure 18: Location of the eight thermocouples with respect to the bottom of the pool

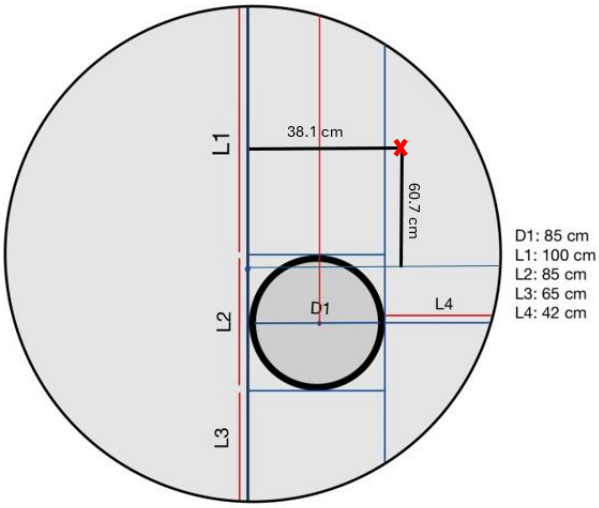

Figure 19: Position of the thermocouple array used to compare the temperature profile of the pool to a CFD model at 50% and 100% power levels. Note: this location is not the same as the location used for estimating the power using heat-balance equations and heat rate calibration (discussed later in Section 3.6 Immersion Heater Calibration).

Each thermocouple channel (CH-1 to CH-8) corresponds to a certain height with respect to the bottom of the pool, and the location of each thermocouple was chosen such that the rise in temperature towards the surface of the pool from free thermal convection could be utilized in the power estimate process. Thus, the location of the thermocouples with respect to the bottom of the reactor pool for CH-1, CH-2, CH-3, CH-4, CH-5, CH-6, CH-7, and CH-8 are located at 0.5 m , 1.0 m, 1.5 m, 2.5 m, 3.5 m, 4 m, 4.5 m, and 5 m respectively. The thermocouple array was used in two instances: (1) obtaining a temperature profile at 50% and 100% nominal power to compare with the temperature profile using a CFD model of the reactor pool (see Figure 20, Figure 21, and Figure 22) and (2) estimating the thermal power using heat balance equations and immersion heater heat rate $\left(\frac{dT}{dt}\right)$ calibration. As for the case with no immersion

heaters, five power levels were used to calculate the thermal power added to the pool at 1.45 kW, 2.90 kW, 6.11 kW, 7.33 kW, and 8.85 kW nominal reactor power (displayed on SIRCIS). The thermocouple array was located at 71.7 cm, radially away from the pool's center, as seen in Figure 19.

Figure 20: Thermocouple array location in the pool (used at 50% and 100% nominal reactor power)

Figure 21: Telescope pole extended fully to precisely attach the thermocouples using aluminum tape

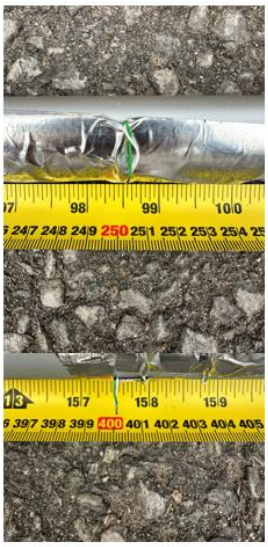

Figure 22: CH4 and CH6 at 2.5 m and 4 m respectively.

3.4 CFD Simulations

ANSYS Fluent was used as the CFD software with parallel meshing. Di Giovanni [10] also used ANSYS Fluent to simulate the reactor core geometry using a CAD developed by CNL and independently simulated by CNL using STAR-CCM+. Both models were ultimately made to compare inlet and outlet temperatures between the two software at different power levels.

As for this thesis, two CFD models were developed, one to simulate the vertical temperature profile of reactor core heating with that using the thermocouple array and the other to assess where the immersion heater aluminum assembly should be located for proper and consistent comparison, which is vital for reactor power calibration. Both CFD models, including the reactor pool, were modelled on a 1:1 scale, with the reactor vessel simplified to a heated cylinder to reduce computational time.

Albadawi et al. [25] presented computational fluid dynamics (CFD) simulations in ANSYS Fluent for the thermal stratification of the water pool outside a small modular reactor (SMR) containment vessel (CV). Their experimental apparatus included a string of thermocouples placed at different depths to validate their CFD model. The simulated power was assigned as an applied heat flux boundary condition, and the model was scaled down to 8:1 to reduce the computational burden. Transient simulation results showed that accurate temperature-time graphs at different depths and power levels could be obtained with the appropriate boundary conditions on the walls of the CV and the reactor pool. The CFD validation step was used as a motive to create a 1:1 CFD model of the SLOWPOKE-2 reactor with geometry simplification to increase computational efficiency. The CFD would give insight into which power levels assigned to the reactor container would produce temperature profiles most accurate to experimental data collected using the thermocouple array.

3.5 CFD Setup

The reactor pool modelled in the CFD simulation consisted of a concrete cylinder, 6 m deep and 2.5 m in diameter, lined with 304 stainless steel and filled with water to a height of

5.4 m. The reactor container, simulated as the source of reactor core heating, was modeled as aluminum and had a diameter of 0.61 m. The exact location of the reactor vessel was measured in the SLOWPOKE-2 facility with respect to the outer radius of the concrete pool and used in the CFD simulation for proper comparison. For context, the CFD model simulating the vertical temperature profile of the reactor core heating utilized only seven thermocouples (excluding CH-2 at 1.0 m). Subsequently, an additional channel (positioned between CH1 and CH3) was introduced for the immersion heater case study, resulting in a configuration with all eight thermocouples.

As for boundary conditions, a constant heat flux boundary condition was used in every iteration based on the surface area of the reactor container and the known neutron flux and nominal power (in W/m^2). Radiation heat transfer was not included in the simulation due to its insignificance in enclosed environments. Table 3 summarizes the boundary conditions used in the ANSYS Fluent simulation of the SLOWPOKE-2 pool [11].

Table 3: CFD Boundary conditions

Pool Wall Heat Flux ($\mathbf{W\,m^{-2}}$)	Free Convection Temperature($\mathbf{^{\circ}C}$)	Convection Constant ($\mathbf{W\,m^{-2}K^{-1}}$)
Adiabatic (0)	19.42	10

Natural convection in the water pool, which arises from the buoyancy in the fluid caused by temperature gradients, was simulated using the Boussinesq approximation. The Boussinesq model was used as solutions converge faster when temperature differences are not

significant [19], which was observed by the relatively minor temperature gradients in the thermocouple apparatus. Thus, the density in this model will be treated as in Eq (6).

Table 4 displays the initial boundary conditions for CFD simulation for half and full nominal power in ANSYS Fluent. The setup for the measurement campaign using the seven thermocouples and the time for measurements is shown in Table 5

Table 4: CFD Initial conditions for half and full power.

Assumed Nominal Power (W)	Volumetric Heat Flux ($W\ m^{-3}$)	Operating Temperature (°C)
8,850 (50%)	898.86	16.82
17,700 (100%)	1797.67	15.35

Table 5: Measurement campaign at different power levels using the seven thermocouples (with no CH-2 in the setup with eight channels)

CFD Reactor Power (%)	Assumed Nominal Operating Power (W)	Measurement Period (s)	Sampling Time (s)
50%	8,850	1800	1
100%	17,700	1800	1

Gravity was also enabled in the negative z-direction with a value of $9.81\,m/s^2$. The operating temperature was set based on the fluid domain's initial bulk temperature. Lastly, due to incompressible and low-velocity flows, the solver was set up with a pressure-based segregated solver using the SIMPLE algorithm, which uses a relationship between velocity and pressure corrections to enforce mass conservation and to obtain the pressure field [26]. The test cases performed to determine the thermal profiles at half and full reactor core heating power are presented for comparison with the thermocouple measurements obtained at the actual half and full nominal reactor powers.

As for the preliminary test case of no immersion heaters, the thermocouple data was sampled every second for each depth and was used to estimate the power based on the heating rate and losses. Two nominal power levels were tested: 50% and 100%. The reactor was operated at each power level for 30 minutes before switching to the next one. The active chillers and water de-ionizer systems were turned off during both runs.

The location and temperature profile of the water in the reactor pool were initialized based on the data collected at different power levels. Initial temperature readings from the thermocouple at half nominal power are displayed below in Table 6.

Table 6: CFD Initial temperature profile for half nominal power.

Channel #	CH-1	CH-2	CH-3	CH-4	CH-5	CH-6	CH-7
Depth (m)	5	4	3	2.5	2	1.5	1
Temperature ($C°$)	15.75	16.21	16.79	16.94	16.94	17.21	17.65

Lastly, the immersion heater case study incorporated initial temperatures arbitrarily ranging between 15 $°C$ to 19 $°C$ and the heat flux (in W/m^2) was set based on their respective surface such that the total thermal power output corresponded to 8.85 kW.

3.6 Immersion Heater Calibration

The location of the aluminum assembly that suspends the immersion heaters in the reactor pool was chosen such that the heating profile of the water would be as close as possible to that of the reactor core. A transient CFD simulation using ANSYS Fluent was employed to observe the effects of reactor nominal half power (8.85 kW) heating from the immersion heaters with 5.4 m of water after 80 minutes. Two models (hereby referred to as Model A and Model B) where the center of the aluminum plate would be located 0.71 m and 0.14 m, respectively, radially outwards from the center of the reactor container (see Figure 23). It is important to note that due to the limitations of available space above the reactor pool from other experiments and instrumentation, the lower right quarter of the cylindrical pool could only be used to lower the aluminum assembly.

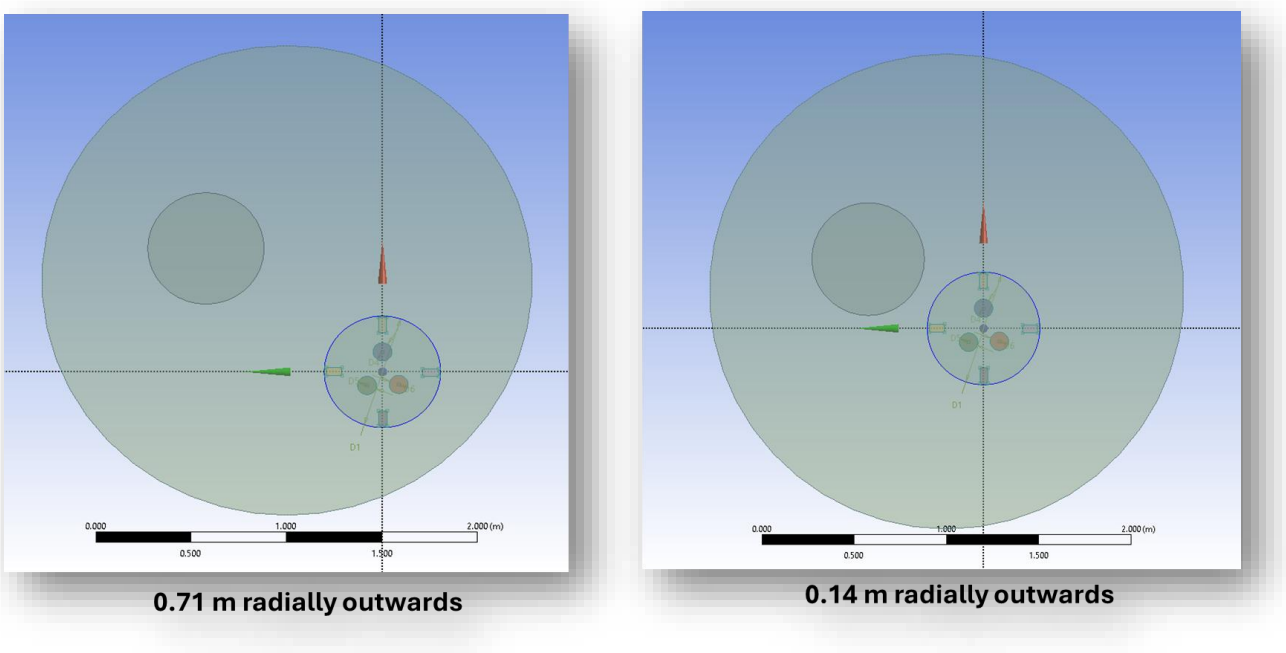

Figure 23: (Left) Model A with the immersion heater plate located 0.71m radially outwards. (**Right**) Model B with the immersion heater plate located 0.14 m radially outwards.

In addition to the location of the thermocouples, it should be noted that the immersion heaters and the nuclear fission inside the core generate heat differently. The reactor core typically generates heat in a concentrated manner, so placing the immersion heaters near the core helps mimic this localized heating pattern, ensuring that the thermal gradients produced by the heaters are more representative of the actual reactor conditions (Model B). When the immersion heaters are 0.14 m radially outwards from the core, the heat transfer mechanisms (both conduction through the materials and convection in the water) are more directly comparable to those present in the reactor.

Positioning the immersion heaters closer to the core would minimize heat losses and reduce external influences, such as upward heat flow within the reactor pool, resulting in a

more accurate calibration of the reactor's thermal power output. Since the primary goal is to calibrate the immersion heater power to that of the reactor core (which is currently estimated using a correlation between an electrical current in the detectors to a neutron flux and then another correlation to the thermal power), replicating the core's heating behaviour is crucial. A similar heating profile would ensure that any thermal feedback, transient responses, and steady-state conditions observed are analogous to those from the reactor core, leading to a more reliable calibration process (see Figure 24).

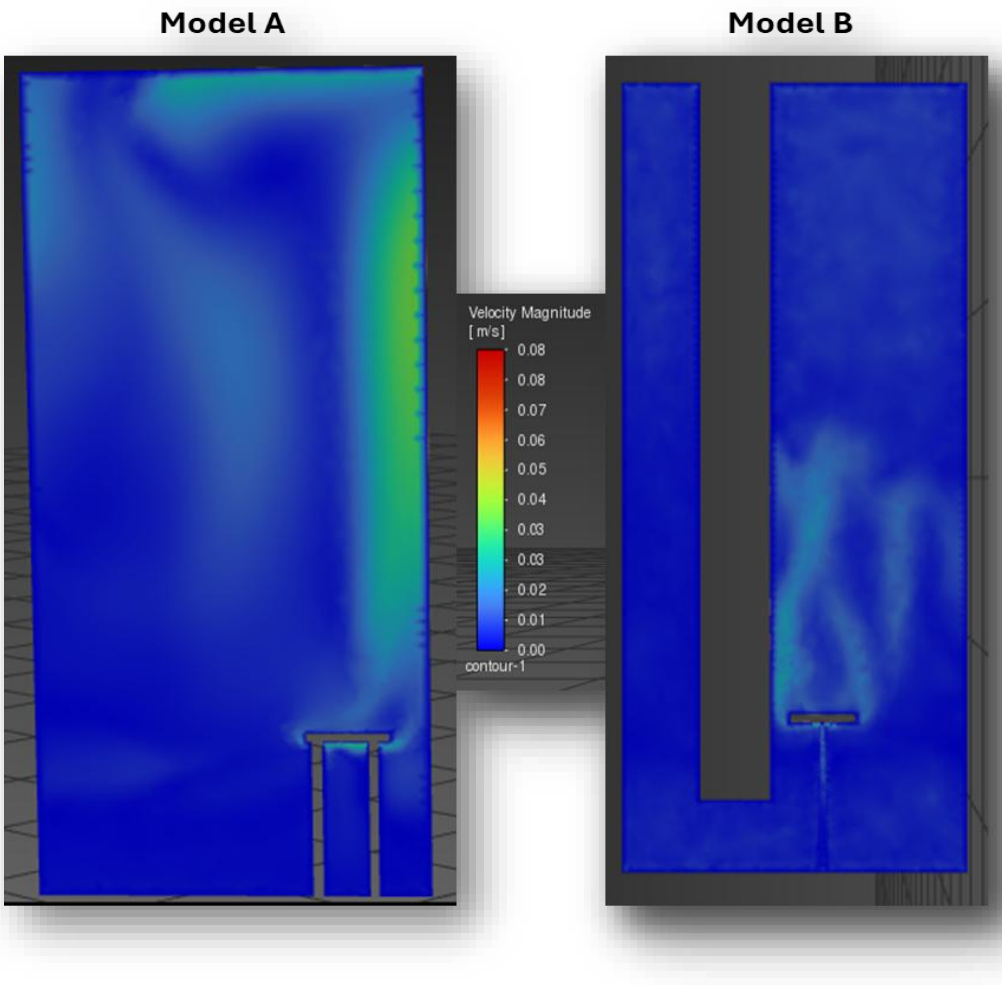

Figure 24: Cross section across the center of the immersion heater plates for Model A and B. Note: the reactor container is visible in Model B only since the cross section crosses through the reactor container.

The transient temperature distributions for Models A and B after 82 minutes reveal key differences in the thermal behaviour of the deionized water pool (see Figure 25). One of the main distinctions is the localized heating observed beneath the aluminum plate in Model A, which is significantly less pronounced in Model B. This variation would directly impact the overall heat transfer efficiency and temperature uniformity within the system, influencing the effectiveness of natural convection and thermal performance. Additionally,

there is a significant concentration of heat in the lower regions, which could lead to localized stratification, where hotter fluid remains confined in specific regions without sufficient buoyancy-driven mixing to distribute the thermal energy effectively (as seen in Model A). This limitation can affect the overall heat dissipation process, potentially leading to thermal gradients that may contribute to inconsistent comparisons between the immersion heater assembly and the reactor core.

Conversely, Model B exhibits a more diffused and evenly distributed temperature profile, particularly in the regions below the aluminum plate. The reduced intensity of heating in this area indicates that placing the immersion heaters closer to the core enhances convective mixing and stratification that would be present when the reactor core is turned on, allowing heat to be transported more effectively throughout the fluid domain. This characteristic aligns with the fundamental design objectives of SMR systems, which emphasize passive safety and effective thermal management to ensure reactor stability under various operating conditions. Ultimately, this resulted in placing the immersion heater assembly as close as possible to the reactor core while still considering the limitation of the area that can be utilized to lower the apparatus. The thermocouple array was placed. 28.5 ± 0.5 cm away from the center of the reactor container and 28.5 ± 0.5 cm away from the center of the aluminum plate.

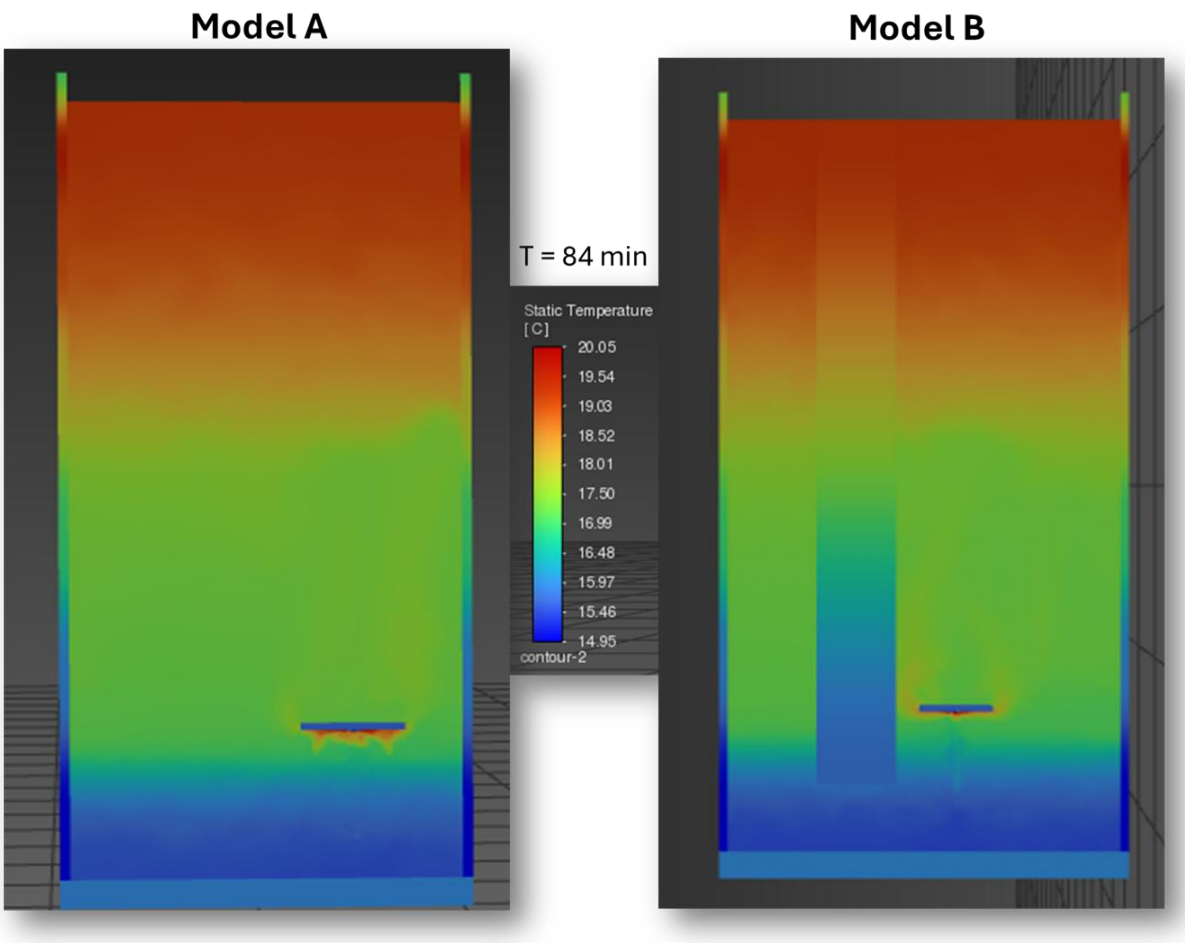

Figure 25: Static temperature (in $°C$) cross section for Model A (Left) and Model B (Right). These results support the conclusion that Model B would provide more accurate thermal distributions in the pool compared to Model A. By reducing localized heating below the aluminum plate and therefore a more even heat distribution, Model B would allow for natural convection pathways and enhancing the overall heat removal process. These factors would collectively contribute to improved reactor efficiency and longevity, making Model B the more favourable design for immersion heater placement in this application.

Another factor that was considered in addition to the location of the immersion heaters, was the height of the coils with respect to the reactor core. Displacing the heater to a different height similar to the reactor core pins could force convection and consequently undesirable stratification. This would ultimately affect the accuracy of experimental results and would lead to discrepancies when compared to theoretical and computational models.

Thus, the bottom of the immersion heater coils is positioned at the same axial height as the bottom of the reactor core to ensure the same heat localization generated using the reactor core (see Figure 26 and Figure 27).

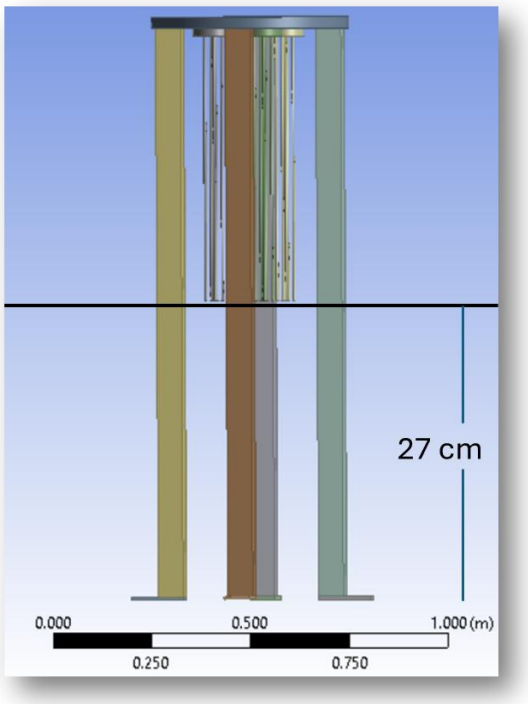

Figure 26: The immersion heater assembly with the bottom of the coils in line with the bottom of the reactor core rods.

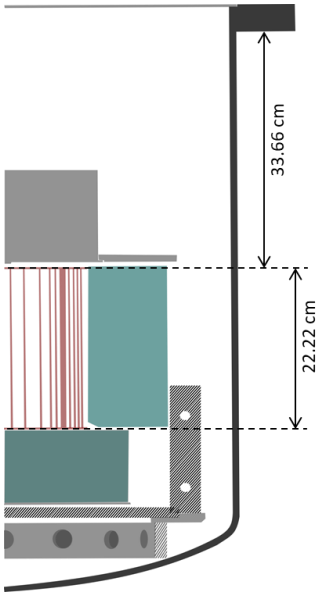

Figure 27: Lower section of the reactor container with reactor core height.

By choosing the location of the aluminum assembly and the positioning of the immersion heater coils relative to the reactor core, the expectation of similar heating rates between the immersion heaters and the reactor core can be justified. The immersion heaters

were deliberately arranged to mimic the spatial heat distribution of the reactor fuel, with their placement on an aluminum plate designed to approximate the reactor's core region.

Lastly, the immersion heaters were positioned such that their distance from the thermocouple string was comparable to that of the reactor core, ensuring that the thermocouples experienced a similar thermal environment regardless of whether the heating source was the immersion heaters or the reactor fuel. Figure 27 displays the relative locations.

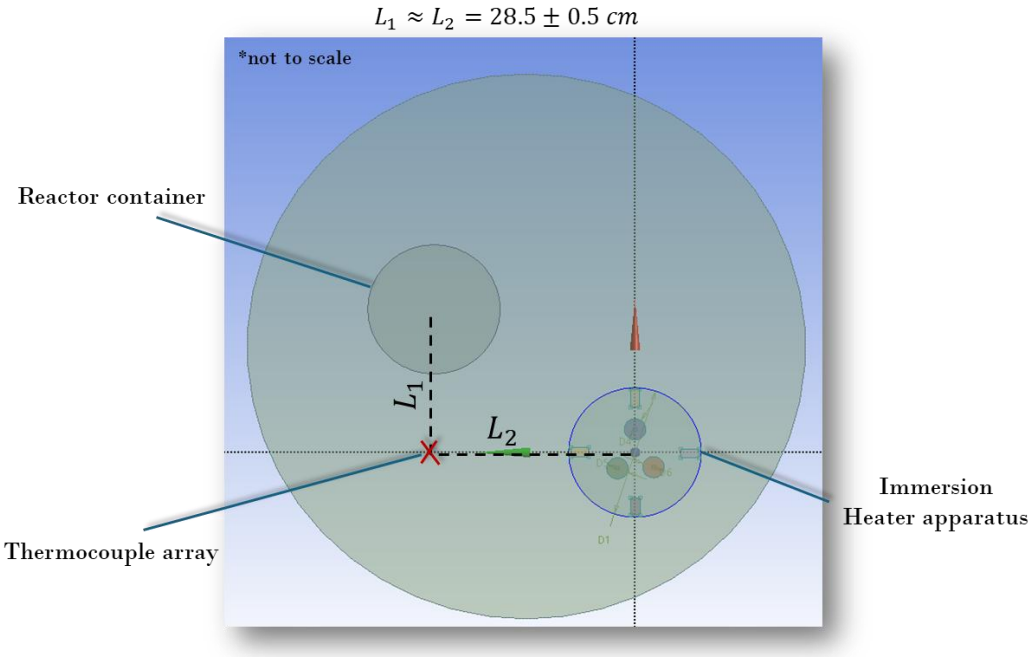

Figure 28: The location of the thermocouple array from the immersion heater apparatus as well as the reactor container.

Using the previously mentioned design setups, the immersion heaters and the reactor core should deposit the same amount of heat by free thermal convection into the same deionized water medium. The temperature rise recorded by the thermocouples is essentially a function of the rate at which heat is added to the surrounding water, meaning that if the

immersion heaters are depositing a known power and producing a measurable heating rate, the same principle should hold for the reactor core. Additionally, the three immersion heaters are fully submerged, meaning there would be no additional heat sinks or conductive pathways that could result in significant heat losses.

In either case, the presence of thermal stratification would not invalidate this comparison but would rather justify the setup further. The thermocouple placement was specifically chosen to capture the gradual temperature increase as heat rises due to buoyancy-driven forces, assuming that the measurements reflect the overall heating of the pool rather than isolated local effects at those heights. The gradual and continuous temperature rise observed during immersion heater operation aligns with the expectations for a system in which heat is steadily accumulating in the surrounding water. Since the reactor's core also deposits heat into the pool via similar mechanisms, it is reasonable to assume that the heating rate observed from the reactor should follow the same trend when the total power input is equivalent.

Finally, the linear relationship between heating rate and power observed in the immersion heater calibration provides further validation (shown in

Chapter 4: Results). Since the immersion heaters showed a clear, consistent trend where the heating rate scaled predictably with power input, the same should hold for the reactor core, regardless of whether it follows the nominal power values that SIRCIS displays. If the heating rate measured from the reactor at a given power level significantly deviates from this trend, it suggests that the reactor's neutron flux-to-power conversion may not accurately reflect the true thermal power being deposited into the pool. This would ultimately strengthen the case for using the immersion heater calibration and theoretical heat-balance estimation as a means of independently verifying reactor power rather than an inferred power estimate.

Given all these considerations, it is expected that the heating rates from the immersion heaters and the reactor core should be similar when operating at the same power levels. Any significant discrepancy would suggest an issue with the way reactor power is currently being estimated, which aligns with the observed findings that the reactor may be producing more power than indicated by its control system.

Chapter 4: Results

This section mainly consists of four sections: (1) vertical temperature profile comparison between the CFD model and the reactor core heating, (2) power estimates using theoretical heat-balance equations, (3) power estimates using heat rate calibration between immersion heaters and reactor core, and lastly, (4) a brief description of utilizing the theory described by van der Ende et al. regarding monitoring reactor fuel use remotely. The data collected using the type-K thermocouple array, immersion heater power meter readings, ANSYS Fluent CFD simulations, and neutron flux measurements will be used to support the conclusions drawn in this thesis.

4.1 CFD temperature profile comparison

Using the temperature profile with the setup that had seven thermocouples instead of eight (with no channel at 1.0 m), a CFD model was employed to compare the temperature profile at half nominal reactor power (8.85 kW) and full power (17.7 kW). Figure 29 and Figure 30 illustrate these comparisons clearly at half and full reactor powers.

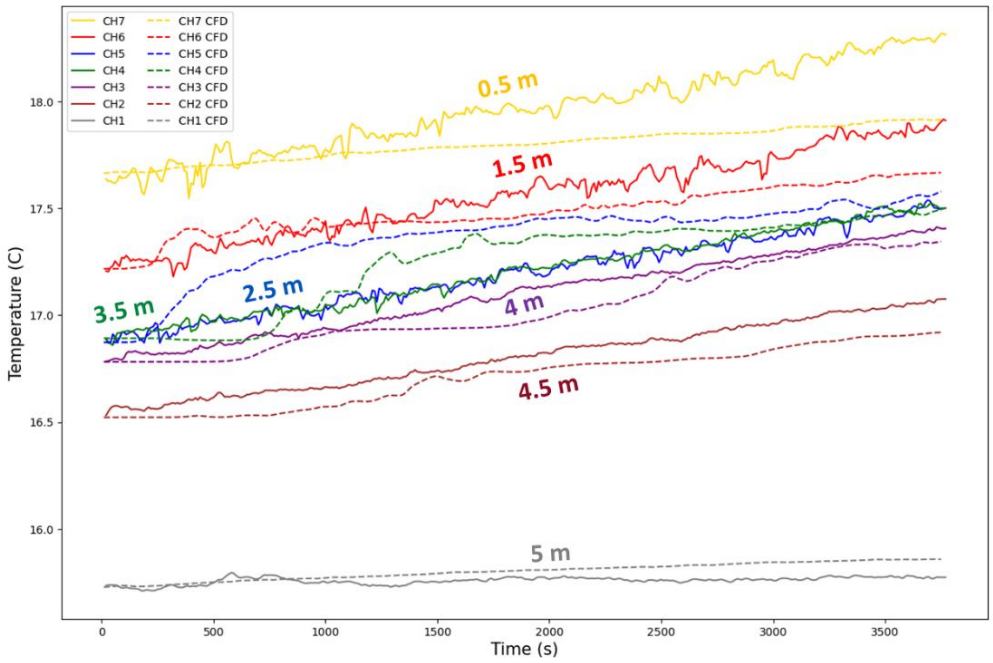

Figure 29: CFD (dashed) and measured (solid) temperature profiles at 0.5 m, 1 m, 1.5 m, 2.5 m, 3.5 m, 4 m, 4.5 m, and 5 m depths for half-power

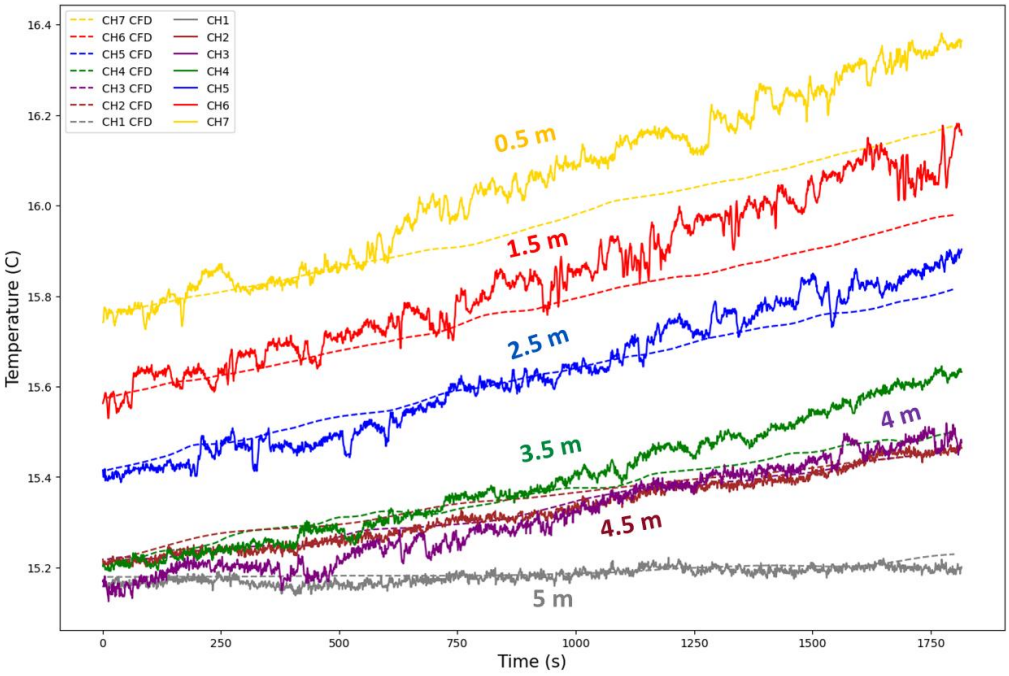

Figure 30: CFD simulation (dashed) and measured (solid) temperature profiles at 0.5 m, 1.5 m, 2.5 m, 3.5 m, 4 m, 4.5 m, and 5 m depths for full power.

At half power, the simulated CFD temperature profiles, set with a defined heat flux boundary condition on the reactor container walls, showed good qualitative agreement but consistently underpredicted the experimental measurements. The measured temperatures across all channels were notably higher, suggesting that the reactor might actually be outputting more heat than initially anticipated by the CFD model, or that the heat loss could be less than that assumed in the model.

This trend became even more apparent at full power, as seen in Figure 30. Here, the difference between measured and simulated temperatures increased further, reinforcing initial suspicions about the increased heating compared to the CFD model with the reactor pool at the same thermal power. This discrepancy prompted a deeper investigation into alternative heat determination methods, as discussed in subsequent sections of this thesis.

Ultimately, these CFD comparisons served as a preliminary estimate of the expected power output at a specific neutron flux. In addition to the theoretical heat balance estimates and the reactor heat rate calibration, a proper conclusion can be made.

4.2 Thermocouple data

The results from the type-K thermocouple measurements, conducted at varying heights using a 7.4 m telescopic pole as outlined in Table 2, are presented in Figure 31 to Figure 40. The temperature evolution over time was recorded for both the nominal reactor power and immersion heater setups at different power levels, including 1.45 kW, 2.90 kW, 6.11 kW, 7.33 kW, and 8.85 kW. The graphs illustrate the temperature variations across all channels as a function of elapsed time, where the time period used for both methods was

determined based on the heat source (Reactor or Immersion Heaters), which had the smaller sample time.

Data collection was initiated either when the immersion heaters were activated, or the reactor reached a specified power level. The thermal response was effectively captured by analyzing only the time interval corresponding to the shortest trial, avoiding potential artifacts resulting from initial low-power or non-equilibrium conditions. For example, if 7.33 kW using Immersion Heaters was sampled for 3 hours but 7.33 kW using reactor power was sampled for 4 hours, the reactor power thermocouple data would be cut to 3 hours to match.

This methodology regarding the time sampling period used for the analysis in both methods essentially improves the accuracy of power estimates and strengthens the reliability of comparisons between both methods. This methodology allows the analysis to emphasize the system's thermal response, minimizing the influence of pre-equilibrium fluctuations or noise present in initial measurements. At 8.85 kW, the temperature profile for both reactor core and immersion heaters exhibited a steady and nearly linear increase over time, indicating a consistent heat input and thermal distribution. Across the eight channels, the temperature rise was observed to range from approximately 16.5°C to 20.5°C in the nominal reactor case and from 15.6°C to 16.8°C in the immersion heater case, while noting the smaller sample time for the case with the immersion heaters where the reactor power at 8.85 kW was temporally adjusted accordingly. The gradients of the temperature curves vary between channels, with Channel 8 showing the highest temperature increase, reaching 20.5°C in the reactor case and 16.8°C in the immersion heater case. The deviation between the two setups suggests differences in heat distribution, with the nominal reactor system generating a more

pronounced temperature increase, which raised suspicion of a higher thermal power supplied by the reactor core than what was displayed. It should be noted that although the temperature profiles do not start exactly at the same initial temperatures for all channels, the amount of energy needed to raise the temperature the same amount should be the same, assuming the water remains in a liquid phase. The immersion heater system exhibited slightly greater scatter in temperature data compared to the reactor, possibly reflecting variations in heat transfer efficiency or minor fluctuations in experimental conditions.

The nominal reactor configuration consistently resulted in higher temperature increases than the immersion heater configuration for essentially all five power levels. The immersion heater system exhibits a more gradual temperature increase, which could be attributed to localized heating effects rather than distributed volumetric heating, as seen from nuclear fission in the reactor core. Channel 1 remains nearly constant and stratified across all power levels and heat sources as it is located underneath both the coils and the reactor core. Thus, it was excluded from both analyses.

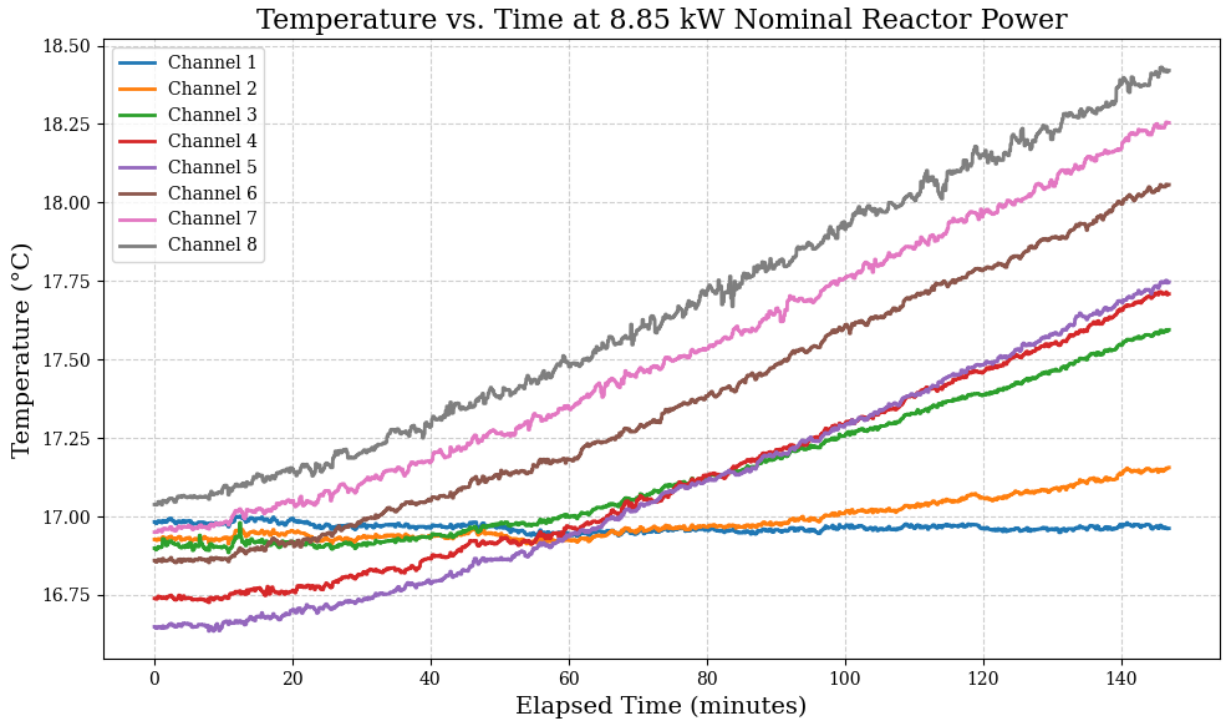

Figure 31: Adjusted temperature profile at half nominal power (8.85 kW) using reactor core.

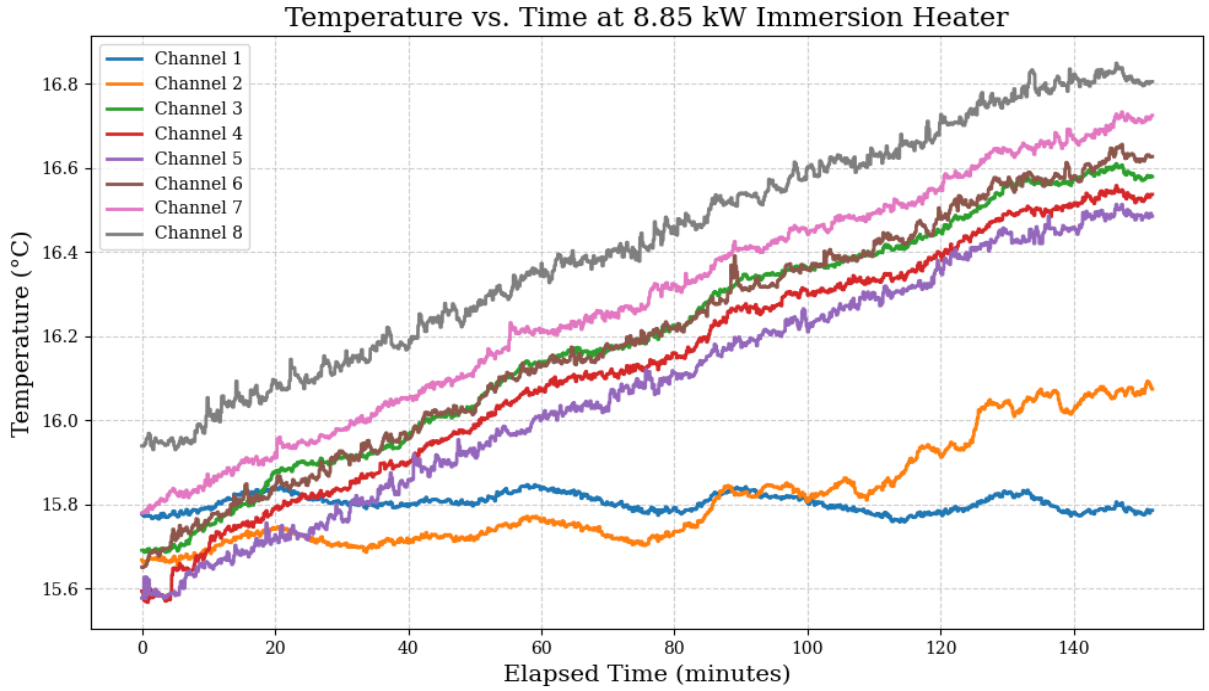

Figure 32*:* Adjusted temperature profile at half nominal power (8.85 kW) using immersion heaters.

At 7.33 kW, the temperature profiles follow a similar trend but with lower overall values due to the reduced power input. The reactor core heating resulted in temperature increases ranging from 15.5°C to 18.0°C, while the immersion heater case saw a range from 14.8°C to 16.2°C. Again, Channel 8 exhibited the highest temperature rise, reinforcing its position as the most thermally responsive measurement point in the system. The temperature profiles at 6.11 kW, 2.90 kW, and 1.45 kW are also displayed below. CH-1 exhibits the same behavior, consistently remaining constant and stratified. In some cases, CH-1 and CH-2 appear to start higher than shallower channels, but this is due to the overnight activation of the deionizing system for the water, which causes mixing at the depths of CH-1 and CH-2. Appendix A: Python script includes additional figures that display the thermocouples when the reactor core and immersion heaters are turned off, but with the deionizer (and chillers) turned on and off.

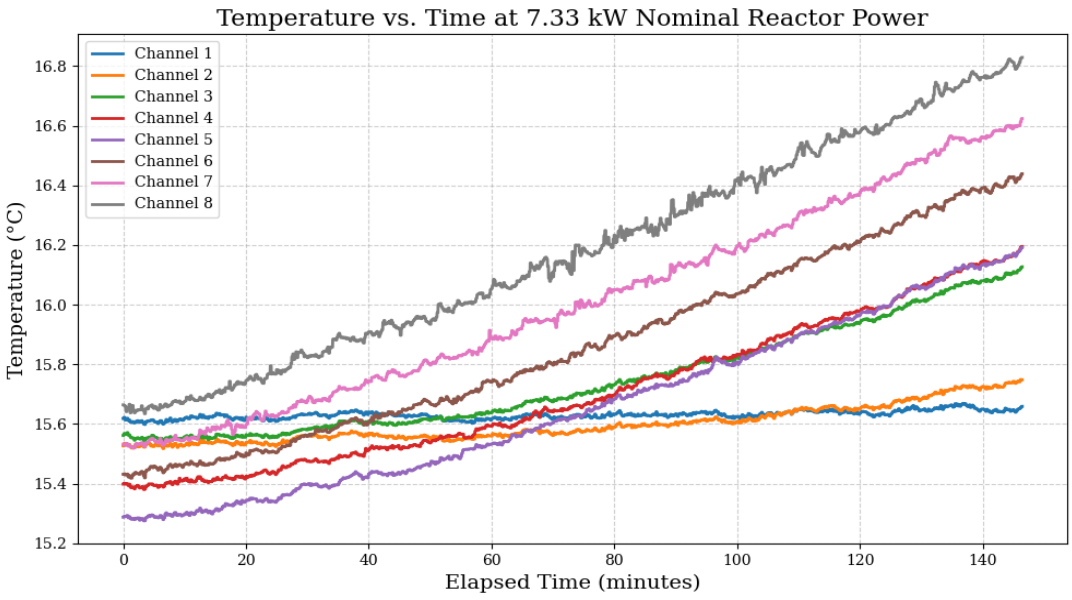

Figure 33: Adjusted temperature profile at (7.33 kW) using reactor core

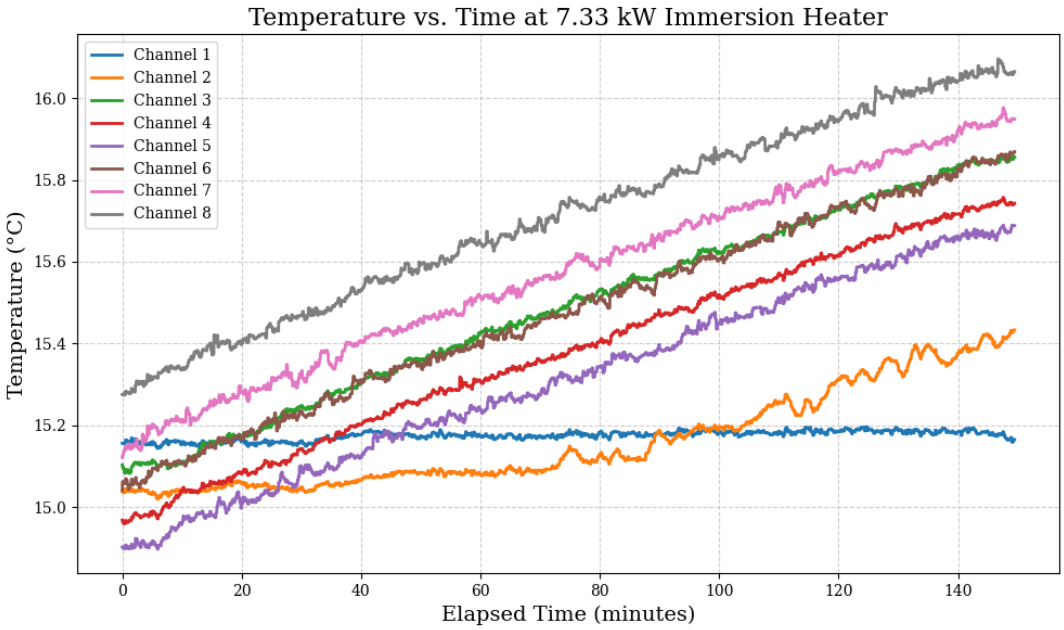

Figure 34: Adjusted temperature profile at (7.33 kW) using immersion heaters.

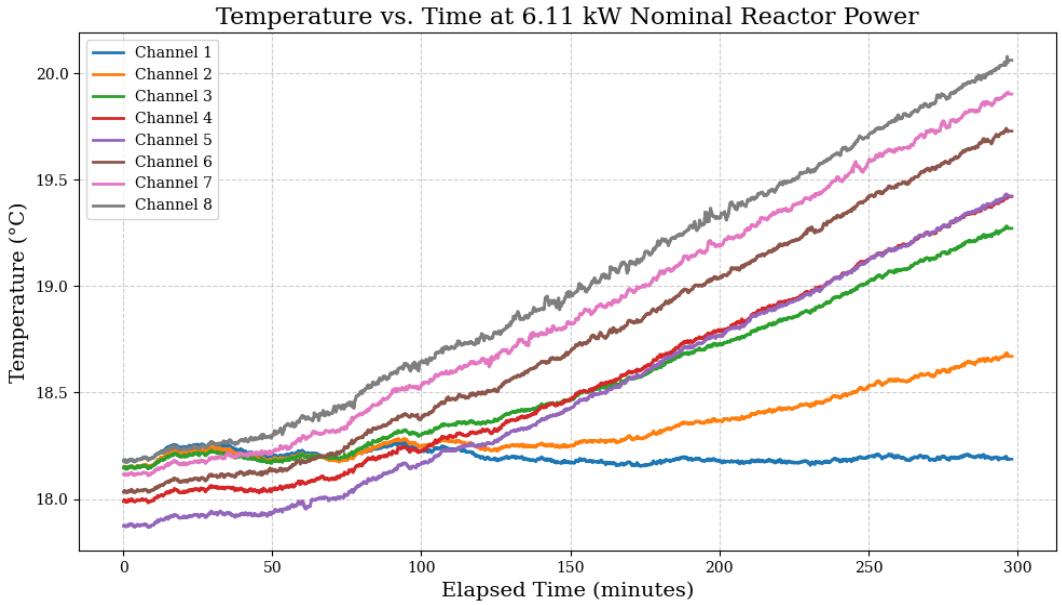

Figure 35: Adjusted temperature profile at (6.11 kW) using reactor core.

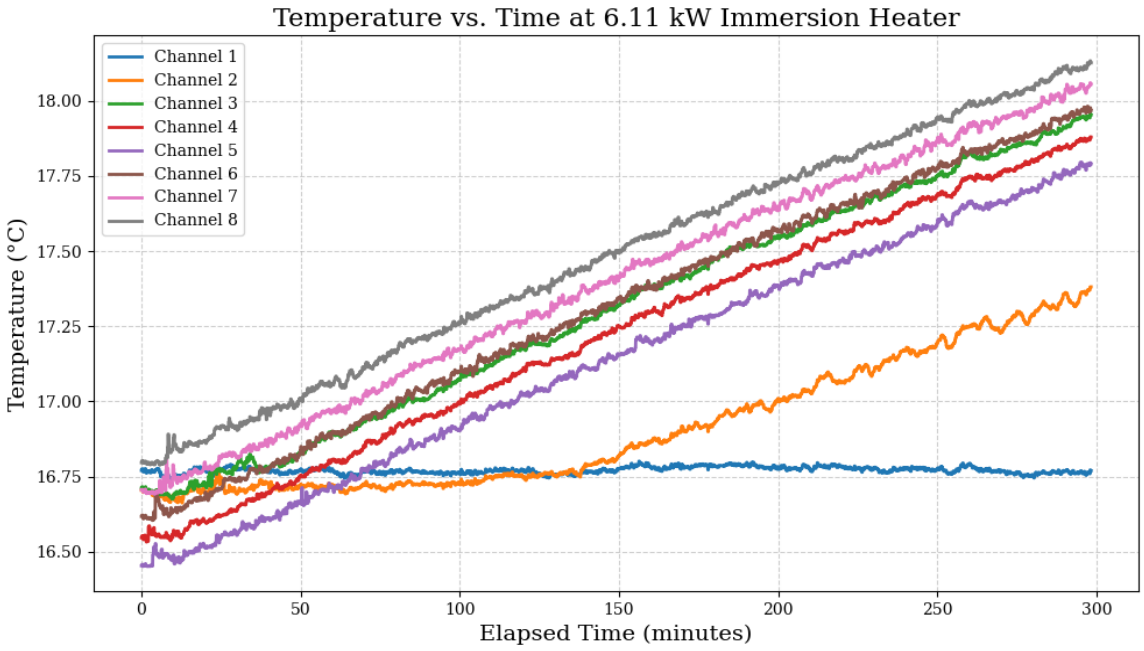

Figure 36: Adjusted temperature profile at (6.11 kW) using immersion heaters.

At 2.90 kW, the temperature distribution across all eight channels shows clear stratification, with Channel 8 (shallowest) reaching the highest temperatures and Channel 1 (deepest) remaining the coolest. This is expected due to the natural convective circulation in the pool, where heat is primarily transferred upwards due to buoyancy forces. As for the nominal reactor test case from Figure 37, The temperature profile shows a gradual increase across all depths, with more uniform heating throughout the pool. Channels 3 to 5, positioned near the height of the immersion heaters, show a moderate temperature rise relative to shallower channels. However, Figure 38 displays how the temperature rise from the immersion heaters is more localized to the mid-to-upper layers, where the immersion heaters were active. Channels 3 to 5 display a more rapid temperature increase, whereas

deeper channels (such as Channel 2) experience a slower response except for channel one, which still consistently stays stratified with no temperature rise.

The temperature gradient between channels is more gradual in the reactor test but more pronounced in the heater test, reinforcing the difference in heat dispersion. A notable difference at lower power levels (such as 1.45 kW and 2.90 kW) is that heat transfer through the pool takes longer, and convective mixing appears less effective due to the reduced buoyancy-driven circulation at lower temperature gradients.

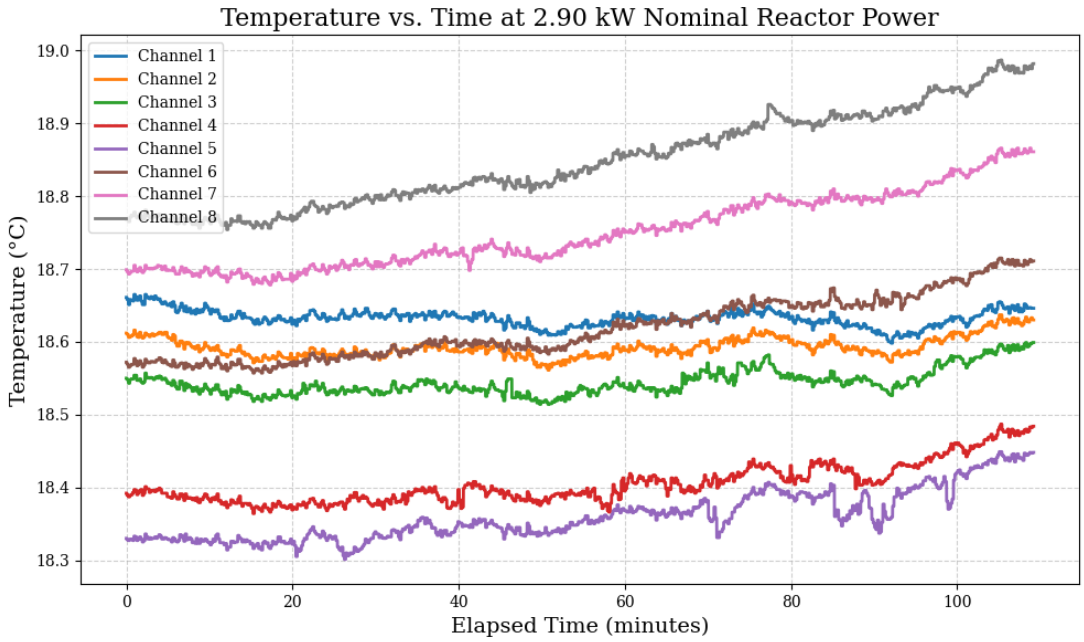

Figure 37: Adjusted temperature profile at (2.90 kW) using reactor core.

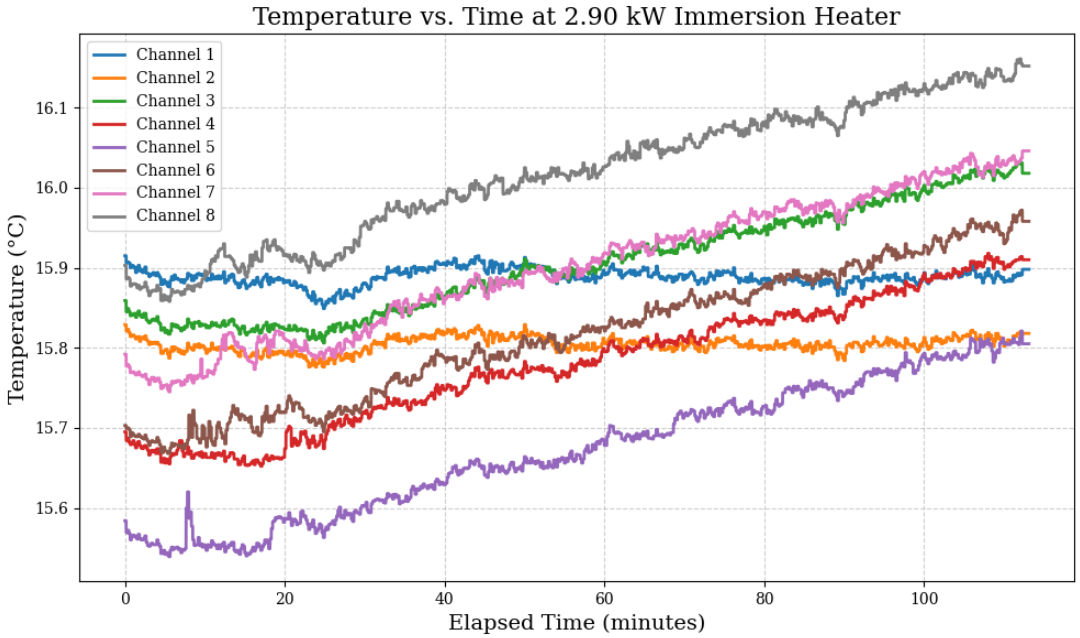

Figure 38*:* Adjusted temperature profile at (2.90 kW) using immersion heaters.

At the lower power level of 1.45 kW, the overall trends are similar but with slower heating rates and a less pronounced temperature separation between layers. As for the case with the reactor heaters turned on, the heat is still relatively well-distributed, with all channels warming gradually over time. While still being less visible for the immersion heaters, the temperature increase is again concentrated in the mid-to-upper layers, with deeper regions showing an even slower response than at 2.90 kW.

Channels 1 and 2 at these power levels start at higher temperatures because the deionizing system must be turned on overnight after ceasing reactor core activity, where forced convection essentially raises the temperature at both stratified layers. With the lack of thermal power compared to being around nominal half power (8.85 kW), the slow heating rate, even after 2 hours, still results in lower temperatures for most channels compared to channels 1 and 2.

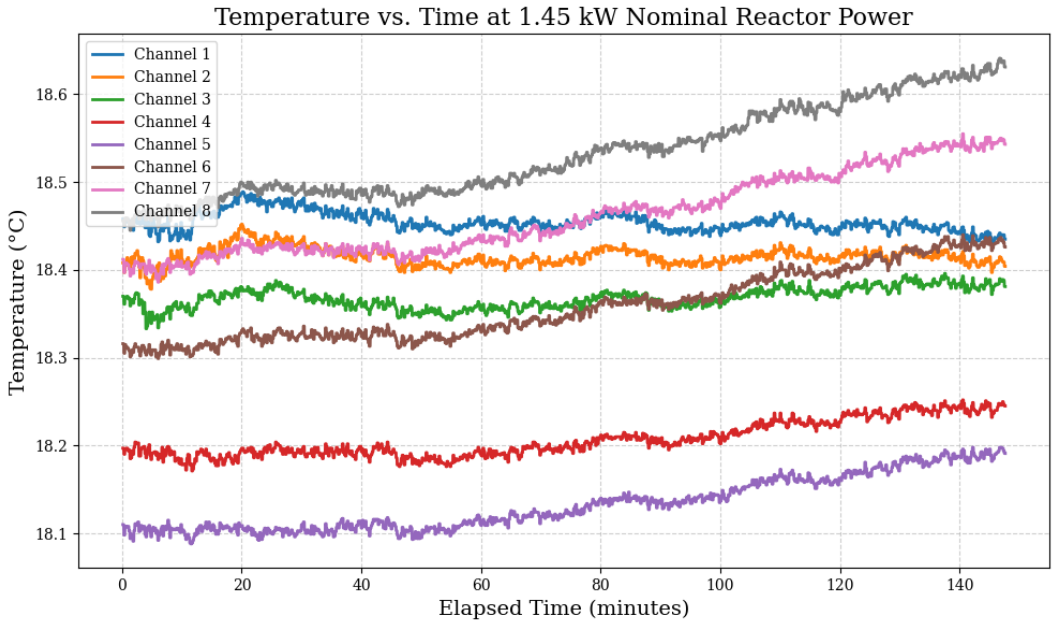

Figure 39: Adjusted temperature profile at (1.45 kW) using reactor core.

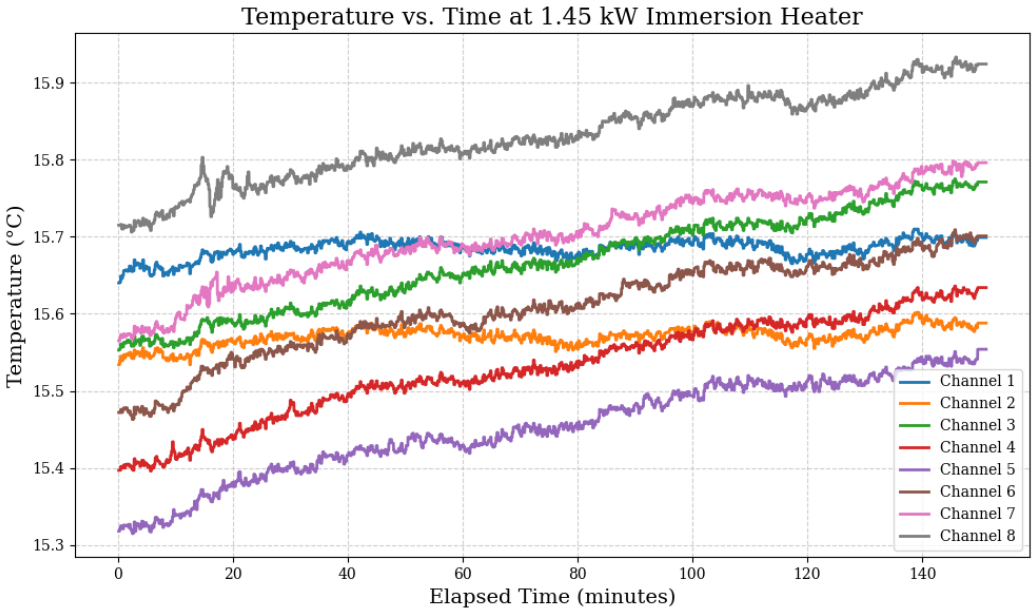

Figure 40 Adjusted temperature profile at (1.45 kW) using immersion heaters.

4.3 Immersion Heater Calibration

This method of estimating the reactor power using immersion heaters corresponds to the heating rate between all eight thermocouples on the aluminum pole to thermal power. The calibration constant is referred to as κ and has units of °C min^{-1}. Here, the constant can be calculated for each power level tested using the immersion heaters (1.45 kW, 2.9 kW, 6.11 kW, 7.33 kW, and 8.85 kW). Table 7 summarizes the results from all five power levels using the immersion heaters and the following correlation:

$$\kappa = \frac{P_{IH}}{\left(\frac{dT}{dt}\right)_{IH}} \tag{14}$$

where P_{IH} is the immersion heater power (in kW) and $\left(\frac{dT}{dt}\right)_{IH}$ is the immersion heater rate of temperature change (in °C min^{-1}).

Table 7: κ constant estimation at various power levels using immersion heaters.

Immersion Heater Power (kW)	Immersion Heater $\mathbf{dT/dt}$ (°C/min)	$\boldsymbol{\kappa}$ constant ($\mathbf{kW \cdot min/°C}$)
$\mathbf{1.45 \pm 0.03}$	0.00079 ± 0.00009	1840 ± 240
$\mathbf{2.90 \pm 0.05}$	0.00170 ± 0.00014	1710 ± 160
$\mathbf{6.11 \pm 0.13}$	0.003850 ± 0.000007	1590 ± 35
$\mathbf{7.33 \pm 0.15}$	0.004480 ± 0.000013	1640 ± 40
$\mathbf{8.85 \pm 0.18}$	0.000540 ± 0.000022	1640 ± 40

Table 8: Summary of results generated from the calibration fit using $\kappa = 1590 \pm 35$

Immersion Heater Measured Power (kW)	Nominal Reactor Power (from SIRCIS) (kW)	Nominal Reactor Power (from κ calibration) (kW)	% Error (Between SIRCIS and calibration)
$\mathbf{1.45 \pm 0.03}$	1.45 ± 0.01	1.59 ± 0.04	8.60%
$\mathbf{2.90 \pm 0.05}$	2.90 ± 0.03	3.27 ± 0.09	11.30%
$\mathbf{6.11 \pm 0.13}$	6.11 ± 0.06	7.38 ± 0.19	17.20%
$\mathbf{7.33 \pm 0.15}$	7.33 ± 0.07	8.40 ± 0.23	12.69%
$\mathbf{8.85 \pm 0.18}$	8.85 ± 0.09	10.63 ± 0.29	16.77%

The κ constant essentially links the measured outputs (voltage, current, temperature gradients, and neutron flux) to the thermal power produced in the reactor or experimental setup. When increasing the reactor power, parameters such as the neutron flux and temperature gradients scale linearly. Therefore, under linear conditions, the ratio of output (neutron flux or temperature gradient) to input (thermal power) stays constant. Additionally, the experimental conditions during all measurements, whether the reactor core or the immersion heaters were turned on, were consistent. These conditions include the thermocouple array and aluminum assembly location, instrumentation setup, neutron detector positioning, and reactor core arrangement.

As per Table 8, all 5 κ estimates for the five power levels are within uncertainty of each other. Thus, to minimize propagated uncertainty in the final power estimation, the calibration constant with the lowest uncertainty in the final power estimation was selected with $\kappa = 1590 \pm 35\ \mathrm{kW \cdot min\ ^{\circ}C^{-1}}$. Using this calibration constant, the heating rate of the thermocouples using the reactor power at different neutron flux setpoints, the same nominal power levels (1.45 kW, 2.90 kW, 6.11 kW, 7.33 kW, and 8.85 kW) can be corresponded to their actual thermal power (as seen in Figure 41) with uncertainty using:

$$P_{reactor} = \kappa \cdot \left(\frac{dT}{dt}\right)_{reactor} \tag{15}$$

$$\sigma_P = P_{reactor}\sqrt{\left(\frac{\sigma_\kappa}{\kappa}\right)^2 + \left(\frac{\sigma_{dT/dt}}{dT/dt}\right)^2} \tag{16}$$

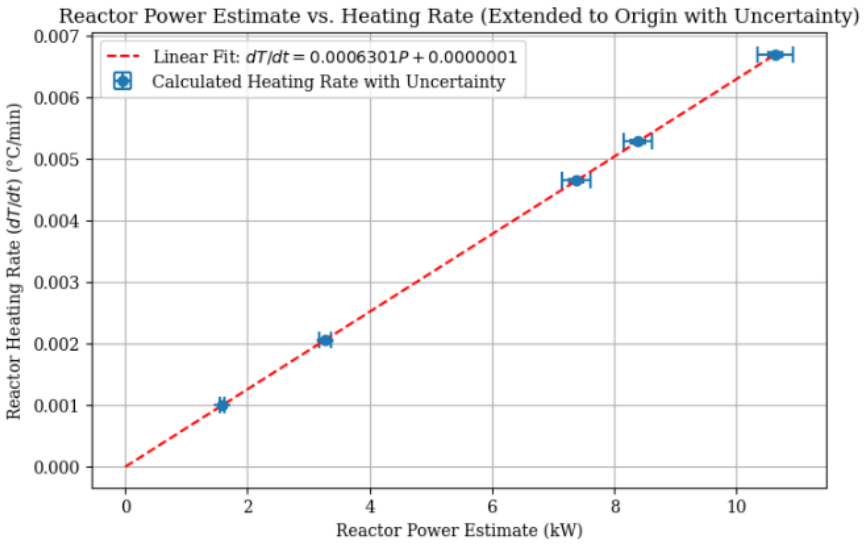

Figure 41: Reactor power estimates using the calibration from the κ constant derived from the immersion heaters.

One of the most interesting results of this analysis is that the calculated reactor power values are consistently 10-20% higher than the power levels recorded in the control room during the experiment. The power levels were set in the control room, using a neutron flux in SIRCIS, at 1.45 kW, 2.9 kW, 6.11 kW, 7.33 kW, and 8.85 kW, yet the heating rate calibration method estimates reactor powers exceeding these values. This discrepancy suggests that the power levels reported by the control room might represent only the nominal or commanded power values rather than the true thermal power output of the reactor. One possible explanation is that additional heat contributions, such as residual thermal energy or secondary heat transfer effects, are not fully accounted for in the control room power readings. Another possibility is that instrumentation uncertainties in the control room

measurements could lead to an underestimation of the actual power being produced. The fact that this discrepancy is systematic across all power levels suggests that it might not be a random error but rather a factor that should be accounted for.

A significant outcome of the regression analysis is the coefficient of determination, $R^2 = 0.99$, which indicates an almost perfect linear relationship between reactor heating rate and power. This methodology further supports utilizing the heating rate for robust power estimation.

Additionally, the y-intercept of the linear fit, $8.39 * 10^{-8}$ °C min^{-1}, is effectively zero, which mathematically implies that when the reactor power is zero, the heating rate is also zero. This is an essential verification step because it aligns with fundamental thermodynamic expectations: if no power is being added or removed to the reactor, its temperature should remain constant over time (including chiller and deionized systems in the pool). The y-intercept is also not artificially offset in any direction, implying no systemic biases.

The accuracy and consistency of this approach between both methods led to an investigation into how reactor power correlates with neutron flux, which is a crucial parameter, in addition to ΔT between the inlet and outlet thermocouples in the reactor container. Both neutron flux and ΔT are actively monitored and logged in the reactor room before and after refuelling. Since reactor power is fundamentally driven by neutron-induced fission reactions, neutron flux should exhibit a direct, proportional, linear relationship with power.

This investigation into neutron flux and power correlation could potentially enhance the ability to use flux as a real-time diagnostic for power estimation, independent of external heating methods. Ultimately, this could provide an additional layer of verification, reinforcing reactor safety and control strategies. Additionally, a calibrated flux-power correlation could allow for finer control adjustments, improving operational efficiency and reducing uncertainties in power estimations. Figure 42 showcases the linear fit of power vs neutron flux (via SIRCIS calibration) as:

$$P = (0.222 \pm 0.004) \times 10^{-10}\phi + (-0.84 \pm 0.07) \quad (17)$$

where P is in kW and ϕ is the neutron flux in n $cm^{-2}s^{-1}$

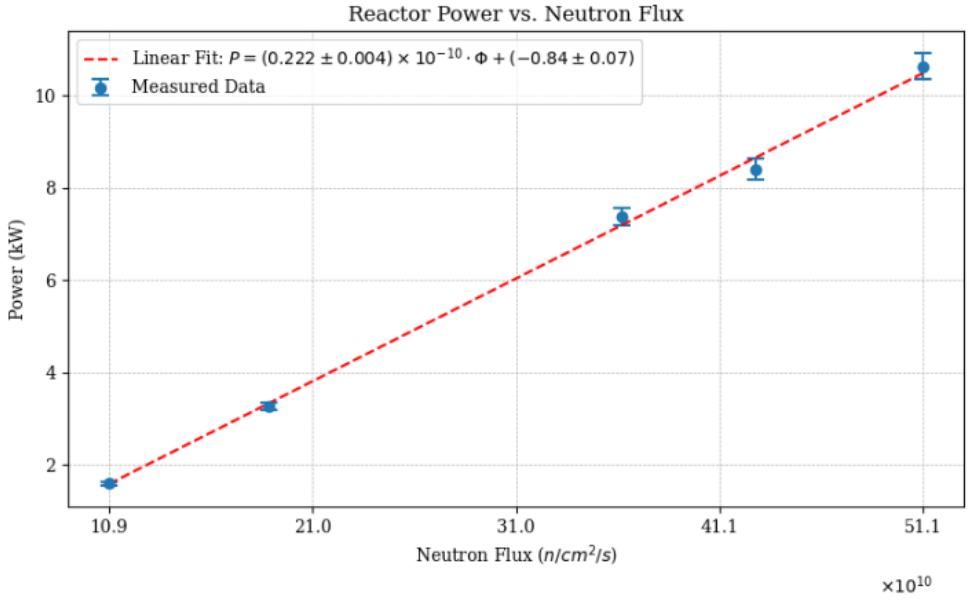

Figure 42: Linear fit of Power (in kW) with respect to neutron flux using the heating rate calibration method

Ultimately, this analysis has validated the temperature-based method as a reliable means of estimating reactor power, potentially revealing a systematic power discrepancy

which led to further investigations into utilizing neutron flux as another potential power estimation tool. These findings provide evidence that reactor thermal response can be quantitatively linked to reactor core power levels, offering a dual-verification approach using both temperature dynamics and neutron flux monitoring.

4.4 Heat Balance Power Estimate

The second approach for estimating reactor power is based on heat-balance equations, which uses heating rate data from thermocouples and applies fundamental thermodynamic principles using a Python script. This method accounts for heat added to the pool, as well as losses due to convection, conduction, and evaporation, resulting in additional power estimates with uncertainty from the reactor core. The results of this method, compared against nominal reactor power values from the SIRCIS monitoring system, are summarized in Table 9.

Table 9: Theoretical estimates of reactor thermal power based on power added and losses.

Nominal Reactor Power (from SIRCIS) (kW)	Nominal Reactor Power (from heat balance eqn.) (kW)	% Error (Between SIRCIS & Heat Balance Calculation)
$\mathbf{1.45 \pm 0.01}$	1.84 ± 0.20	21.19 %
$\mathbf{2.90 \pm 0.03}$	3.34 ± 0.17	13.17 %
$\mathbf{6.11 \pm 0.06}$	7.08 ± 0.17	13.70 %
$\mathbf{7.33 \pm 0.07}$	8.27 ± 0.16	13.70 %
$\mathbf{8.85 \pm 0.09}$	10.25 ± 0.16	13.65 %

In addition to the heat rate calibration method, the heat balance method also overestimates the SIRCIS reactor power estimates, with deviations ranging from 13.17% to 21.19%. The largest discrepancy occurs at 1.45 kW, where the heat balance method predicts 1.84 kW, while the smallest deviation is at 8.85 kW, where it estimates 10.25 ± 0.16 kW at "half-power". Uncertainty in the power estimates arises from incorporating errors in temperature gradient measurements, volume estimations, and loss coefficients. The total uncertainty in power estimates ranges from 0.16 kW to 0.20 kW, reflecting the cumulative effect of measurement errors and assumptions in loss modelling. The approach to uncertainty estimation accounts for measurement errors and estimated loss coefficients but does not fully capture systematic errors related to model assumptions. For example, the conduction loss model assumes uniform thermal contact between layers, but real-world conditions may

involve variable heat transfer rates. Similarly, the evaporation loss model is based on empirical correlations that may not fully reflect experimental conditions. A sensitivity analysis, including the possible ranges for the constants and formulas used in the power losses formula, could be employed to confirm the insignificance. So, while there is some inherent uncertainty in how heat losses are estimated due to approximations in convection coefficients, material conductivities, and empirical evaporation models, this additional uncertainty is relatively minor. Specifically, these factors contribute only marginally to the total error range, as demonstrated in Figure 43, which showcases the relative magnitude of losses affecting each channel with uncertainty. As previously mentioned, only CH-8 would have convection and evaporation losses as opposed to only conduction for the other channels.

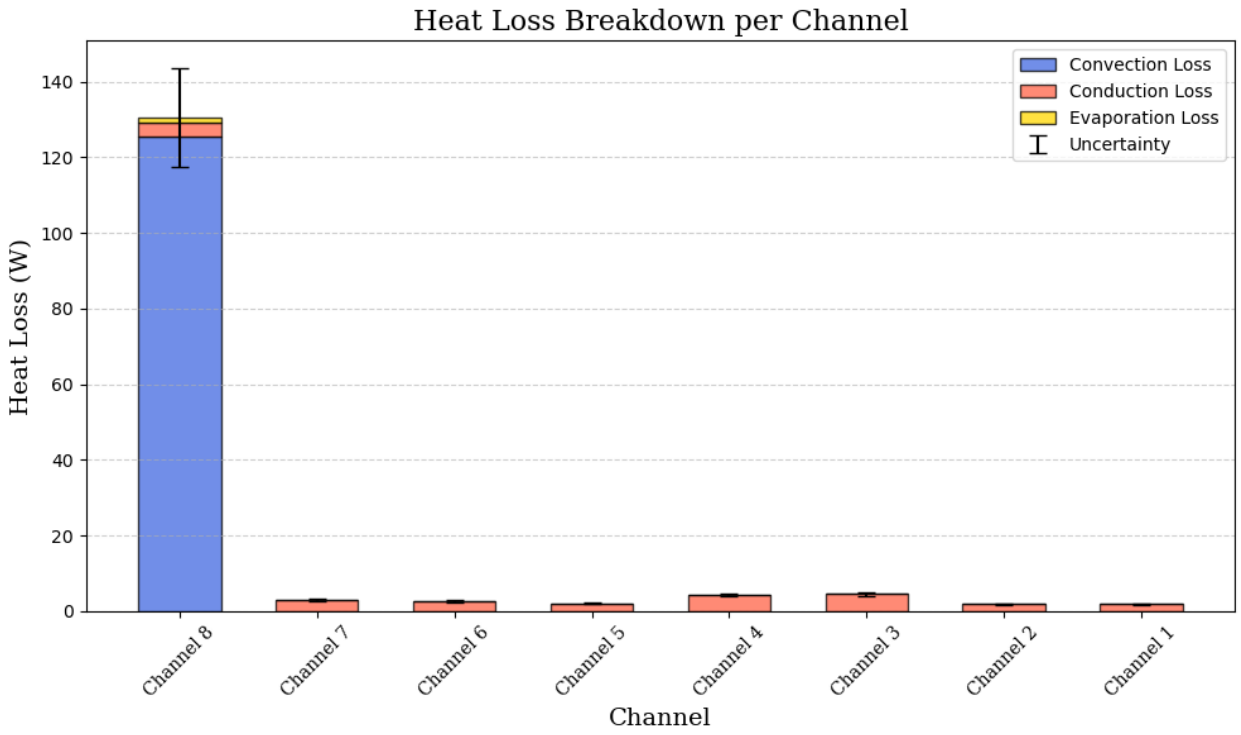

Figure 43: Power losses for each channel and the contribution from convection, conduction, and evaporation.

Both methods can now be seen as complementary to each other. The κ calibration method inherently corrects for unmodeled heat losses by tuning the coefficients based on experimental calibration and expectations, while the heat-balance method offers a structured breakdown how the energy is distributed, explicitly accounting for convection, conduction, and evaporation losses. Ultimately, this affects the experimental model of the reactor core by reducing its bias and justifying the use of both methods as a more refined model, which essentially creates an additional method for estimating reactor power (see Table 10).

Table 10: Summary of the SLOWPOKE-2 SMR thermal power output from two methods: Using theoretical heat balance equations, and heating rate calibration using immersion heaters.

Nominal Reactor Power (from heat balance eqn.) (kW)	**Nominal Reactor Power (from κ calibration) (kW)**	**% Difference between Heat balance eqn. method vs κ calibration method**
1.84 ± 0.20	1.59 ± 0.04	%14.6
3.34 ± 0.17	3.27 ± 0.09	%2.1
7.08 ± 0.17	7.38 ± 0.19	%4.1
8.27 ± 0.16	8.40 ± 0.23	%1.6
10.24 ± 0.16	10.63 ± 0.29	%3.7

4.5 Neutron Flux Analysis

This section provides a comprehensive and technically detailed analysis of the neutron flux behavior before and after the refuelling of the SLOWPOKE-2 reactor at RMC. Specifically, it examines how the correlation between reactor thermal power and inlet-outlet coolant temperature difference (ΔT) can be used to estimate thermal power output of a given ΔT before refuelling, which is one of the only quantities consistently measured and calibrated before refuelling by SIRCIS. The importance of this relation lies in its application for estimating reactor thermal power in scenarios where direct calorimetric measurement is impractical or unavailable, as well as for the assessment of the theory provided by van der Ende et al., which states that SMRs can be monitored remotely at stand-off distances with large area neutron detectors [2]. Ultimately, this would provide an evaluation for the change in fissile content between the old and new core. The analysis integrates a power-law fit to temperature-derived power estimates, computation of the weighted isotopic composition (WIC), and comparison of the measured change in neutron flux to power ratio (NFPR) to the corresponding change in WIC. A thorough discussion of contributing discrepancies is provided to explain observed discrepancies between the experimental NFPR and calculated change in WIC. All results and discussions are consistent with the thesis objective to validate a non-invasive power calibration methodology and assess isotopic changes using remote neutron flux measurements.

4.5.1 Power Law fit

The experimental methodology begins by analyzing the relationship between reactor thermal power and the temperature difference across the core, recorded via inlet and outlet thermocouples in SIRCIS. The uncertainties derived from both the slope and the intercept were carried over to the following power and WIC calculations. Thus, the validity and consistency of this relationship with uncertainty propagation form the basis for comparing reactor conditions before and after the core refuelling event. See Table 11 and Table 12 for the data demonstrating the power law correlation.

Table 11: ΔT between the inlet and outlet temperature averaged over the same time period used for the heat-balance estimate for the power.

Date (2025)	SIRCIS Power (kW)	ΔT(°C)	δ ΔT(°C)	Power (kW)	δP (kW)
Feb 26th	7.33	13.296	0.003	8.40	0.23
Feb 28th	6.11	11.714	0.004	7.38	0.19
Mar 3rd	8.85	14.394	0.003	10.63	0.29
Mar 4rth	3.11	7.928	0.001	3.27	0.09
Mar 5th	1.45	5.401	0.001	1.59	0.04

Table 12: Log-log data used to obtain the power law correlation for the power.

Log(P)	δ Log (P)	Log (ΔT)	δ Log (ΔT)
0.924	0.012	1.12	9E-05
0.868	0.011	1.07	1E-04
1.027	0.012	1.16	8E-05
0.515	0.012	0.90	4E-05
0.201	0.011	0.73	5E-05

A log-log linear regression was derived from experimental data in Tables 11 and 12 collected in Jan – March 2025, shown in Figure 44. The linear regression equation indicates that the relationship between power and ΔT approximately follows a power-law with an exponent of 1.92±0.06, implying a nonlinear (near-quadratic) behavior. This is consistent with expectations from heat transfer theory in systems where convection dominates over conduction [27].

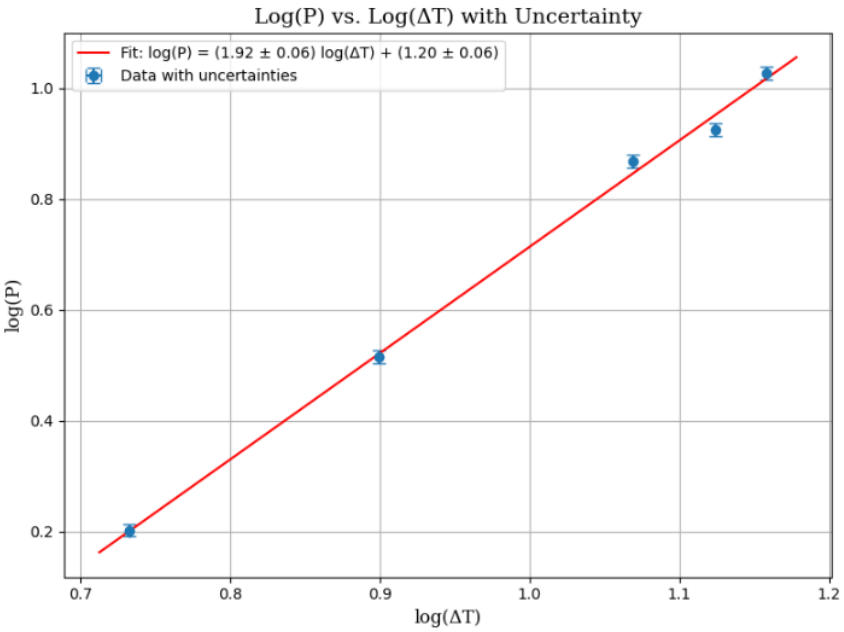

Figure 44: Linear plot used to deduce the correlation between P and ΔT and is assumed to be applicable before refueling.

4.5.2 NFPR Before and After Refueling

The fitted power law in Figure 44 was applied to neutron flux data gathered using two distinct detectors (B10+ and He-3) before and after the September 2021 refuelling. Since the reactor powers for the He-3 and B10+ count rate measurements are not identical to the powers at which measurements were taken with the immersion heater method, or the heat balance method, the log-log correlation between P and ΔT was be used to estimate the reactor powers for each of the He-3 and B10+ measurements, based upon what ΔT was at each measurement. The NFPR provides a normalized measure of neutron flux per unit power that, according to Equation (*1*), serves as an indirect indicator of fissile content (WIC). The calculated values are summarized in Table 13.

Table 13: Power estimates at different mean count rates for B10+ and He-3 detectors with WIC estimates before and after refuelling

Before/After Refueling	ΔT (°C)	Detector	Mean Count Rate (cpm)	Power (kW)	NFPR (cpm/kW)
Before	15.252 ± 0.004	B10+	12.3 ± 0.4	11.63 ± 0.16	1.06 ± 0.04
		He-3	31.2 ± 1.5		2.68 ± 0.05
After	14.651 ± 0.004	B10+	11.64 ± 0.19	10.77 ± 0.16	1.08 ± 0.02
		He-3	29.5 ± 0.5		2.74 ± 0.02

The uncertainty in the NFPR depends on two factors: uncertainty in the count rate and uncertainty in the power estimate. The count rate uncertainty was taken as the standard deviation of the mean, while the power uncertainty was propagated from the log-log fitting using the relation:

$$\delta P = P \ln(10)\, \delta(\log(P)) \tag{18}$$

with:

$$\delta(log(P)) = a \frac{\delta(\Delta T)}{\Delta T\, ln(10)} \tag{19}$$

where a is the slope of the log-log fit, and $\delta(\Delta T)$ is the uncertainty in ΔT. Thus, the percentage change in NFPR before and after refueling can now be estimated, which is shown in Table 14.

Table 14: Experimental estimates for the % change in WIC before and after refuelling compared to simulated estimates.

	NFPR / WIC
B10+ Detector	$(2 \pm 4)\%$
He-3 Detector	$(2 \pm 2)\%$
CNL WIC Estimate (Using Monte-Carlo simulations)	-1.95 %

4.5.3 Comparison of Change in NFPR with Change in WIC

The WIC can be estimated from the fissile isotopic composition estimated from SLOWPOKE simulations [28, 29]. The said simulations allow one to calculate the change in total U and Pu in-core mass when changing out the original core at its discharge burn-up for a new fresh core. From this information, the relative change in WIC is computed from

Equation (*1*) to be -1.95% [10]. According to Equation (1), the corresponding percentage change in NFPR should be equal to the percentage change in WIC. As can be seen from Table 14, the percentage change in NFPR is comparable in magnitude to the percentage change in WIC, but opposite in sign.

The unexpected positive change in NFPR, in comparison with the negative percentage change in WIC, can be accounted for by several plausible factors. First, the power-law fit in Figure 44 assumes that both the exponent and intercept in the log-log equation remain the same before and after refuelling. However, while the exponent reflects physical behavior that remains the same (such as convective heat transfer), the intercept may vary due to geometric and material changes in the core. Since the WIC calculation is sensitive to power estimation, even small changes in the intercept could lead to systematic bias in the before/after comparison.

Additionally, the two low-power data points heavily influence the power-law exponent (1.92 ± 0.06). Thus, the exponent might be overestimated if these points are subject to high uncertainty or noise. A lower exponent (closer to 1) would result in a smaller power increase with ΔT and therefore a lower WIC after refuelling, which would align with predictions. Thus, data sparsity and noise at low powers could significantly skew the fitted relationship.

Configuration changes in the reactor core following physical changes after refuelling may also contribute to the observed NFPR behavior. Prior to refuelling, the overhead shim tray contained ~4.4 cm of beryllium shims, which may have absorbed neutrons and reduced

detected count rates. Post-refuelling, the shim tray was empty, leading to a higher observed neutron flux. The presence of shims may also have impeded heat transfer, thereby influencing the measured ΔT and skewing power estimates, relative to when the shim tray was empty. The new core also had fewer fuel pins, which changed the overall configuration of the pins in the fuel cage. This change likely altered the moderator-to-fuel ratio and the overall thermal-hydraulic profile, affecting both heat generation and neutron transport.

Together, these effects suggest that while the power-law model is a useful tool, it is sensitive to systematic configuration changes that must be accounted for when comparing data across major physical transitions such as refuelling.

Chapter 5: Conclusion

The goal of this thesis was to address two primary challenges related to the RMC SLOWPOKE-2 SMR, specifically, (1) establishing a reliable and robust method to measure the reactor thermal power and (2) an in-depth understanding of how changes in the reactor's fissile content occurred following the refuelling to the new core that occurred in September 2021. Ultimately, both tasks would result in a stand-off monitoring system that would allow for a more efficient method of adhering to the current guidelines set by the IAEA, which require the loss of Pu, HEU, and U-233 in irradiated fuel to be detected in under 90 days [13]. This monitoring system would ultimately decrease the risk of nuclear fuel proliferation, which would help to ensure the peaceful use of nuclear materials.

Previously, Di Giovanni [10] and CNL created CFD models of the SLOWPOKE-2 SMR core using ANSYS Fluent and STAR-CCM+, respectively, but the uncertainty with the location of the outlet thermocouple introduced a challenge on the ability to calibrate the difference between inlet and outlet thermocouples temperatures in the reactor container to a thermal power. Alternatively, by using an immersion heater assembly with a power that can be measured using power meters and an array of vertical thermocouples, two methods for power estimation could be used: immersion heater heat rate (dT/dt) calibration with reactor thermal power and the use of heat-balance equations to determine the power added to the reactor pool.

For the immersion heater heat rate (dT/dt) calibration method, three immersion heaters (two 1.5 kW and one 6 kW) were selectively turned on and off using a junction box

containing three switches that were wired to an outlet (line side) and to their respective immersion heaters (load side) on the other side. In total, five power levels could be compared with the reactor core power: 1.5 kW, 3 kW, 6 kW, 7.5 kW, and 9 kW. Currently, in the reactor room, by using SIRCIS, the reactor power is set by assigning a neutron flux, which would lower or raise the cadmium control rod until the desired neutron flux is reached. The electrical current in the detector is correlated to a neutron flux, which is then correlated to thermal power based on calibrations performed on the old core before refuelling.

The thermocouple array with eight channels was used to obtain a vertical profile of the heating at eight different depths for proper calibration. A CFD model was also employed to assess the most appropriate location for the immersion heater assembly, such that it would have a heating profile similar to that of the reactor's core. Ultimately, the immersion heater assembly was lowered and moved as close as possible to the reactor container where both the center of the immersion heater aluminum plate and the reactor container vessel were at a distance of 28.5 ± 0.5 cm away from the thermocouple array. The calibration constant for each power level was determined to be within uncertainty to each other for the immersion heater and the estimate with the smallest uncertainty was chosen at $\kappa = 1590 \pm 35\ \mathrm{kW/^{\circ}C}$. Voltage probes and current clamps were used to estimate the power of the immersion heaters at each step, and the total power was determined in SIRCIS to allow the reactor core to reach the same nominal thermal power output. Using the calibration constant with the smallest uncertainty, the thermal power output of the reactor based on the heating profile obtained from the thermocouple array was estimated for each power level.

Interestingly, estimates for the reactor power values were consistently 10% - 20% higher than what was being recorded in the control room. For example, at half "nominal" reactor power, the power was estimated to be (10.24 ± 0.15) kW as opposed to (8.85 ± 0.13) kW. The discrepancy suggests that the power levels reported by the control room might represent only the nominal or commanded power values rather than the true thermal power output of the reactor. This led to an investigation into obtaining a neutron flux and power correlation, which would enhance the ability to use flux as a real-time diagnostic for power estimation, independent of external heating methods. The linear fit for power as a function of neutron flux was $P = (0.222 \pm 0.004) \times 10^{-10}\phi + (-0.84 \pm 0.07)$ which resulted in a full nominal power at (20.2 ± 0.3) kW at a neutron flux of $10^{12}\ n\ cm^{-2}\ s^{-1}$.

The other method utilized a Python script that outputs the expected power output from the heating rate of 8 thermocouples in addition to estimates for losses at each slice. Similarly, the power estimates also overestimated those from SIRCIS in the control room with deviations ranging between 13.17% to 21.19%, with the largest discrepancy at 1.45 kW where the heat-balance method predicts 1.84 kW, while at half nominal power, the script estimates (10.6 ± 0.2) kW. The uncertainties in the heat-balance estimates arise from errors in the type-K thermocouple measurements, volume estimations, and loss coefficients. Both methods can be seen as complementary to each other, where the kappa calibration method corrects for unmodeled heat losses by tuning the coefficients based on experimental calibration and expectations, while the heat-balance method offers a structured breakdown of how the energy is distributed, explicitly accounting for convection, conduction, and evaporation losses. As demonstrated in Table 10, the two methods provided power estimates

that were in close agreement with each other, with four out of five power estimates agreeing within 5%, and just the low power estimate agreeing within 15%. Ultimately, this affects the experimental model of the reactor core by reducing its bias and justifying the use of both methods as a more refined model that estimates the reactor power based on in-core neutron flux and temperature measurements in the reactor pool.

The neutron flux analysis has attempted to demonstrate the effectiveness of using a power-law correlation between reactor power and ΔT for indirect power estimation and fuel monitoring. The analysis quantified the NFPR before and after refuelling, identified a small yet consistent positive shift in measured NFPR, and clarified this deviation from a predicted negative change in WIC through a combination of model assumptions, fit sensitivity, and physical changes to the reactor.

Ultimately, the neutron analysis estimates showed some reliability for the remote monitoring approach, while emphasizing the need for cautious interpretation when comparing across reactor configurations. Continued collection of low-power data, improved uncertainty quantification, and future simulations incorporating physical geometry changes will further refine these findings.

Chapter 6: Future Work

Recommendations from this thesis will consist of experimental setup adjustments as well as additional measurements that could ultimately enhance the fuel monitoring capabilities of the RMC SLOWPOKE-2 SMR. The temperature profile of the reactor pool is essential in understanding how the calibration using the immersion heaters and the heat balance equations estimate the reactor thermal power.

A string of eight type-k thermocouples was used where an aluminum plate would stabilize the array such that the position could be fixed. However, obtaining a more detailed temperature profile would require an underwater motorized platform that could radially sweep the reactor pool to observe any unexpected heating rates above or around the immersion heaters and reactor container. Wireless thermocouples could also be attached to the aluminum rod to increase the number of volumetric slices used for both the immersion heater calibration and the Python script. In addition to the experimental and theoretical model of the reactor pool, the radial temperature profile can also be used to calibrate CFD models of the reactor pool at different power levels.

Currently, thermal power analysis is based on steady-state conditions, but reactor operations do involve dynamic changes such as power ramp-up and transient conditions. Thus, development of a predictive model incorporating reactor kinetics and feedback effects should be taken into consideration. Future research should explore time-dependent modelling of reactor thermal response during startup and shutdown as well as transient analysis of neutron flux and its effect on real-time power estimation.

Tracking calibration drift from the immersion heaters by developing standardized calibration protocols and repeatability measurement campaigns is also crucial for implementing both methods for reactor thermal power monitoring. As for the sensors used in the experimental apparatus, software-controlled calibrations that automate checks on sensor accuracy, especially when repeated measurements are required, should be performed to confirm initial findings.

As for the WIC estimates, advanced simulation codes such as TRIAD or MCNP could be used to estimate the fuel burnup and isotopic depletion of the old core, which would offer a higher level of accuracy by accounting for variables like neutron cross-section, fuel behaviour, and reactor dynamics. Additionally, using the preliminary estimates that this thesis provides, future research could focus on integrating real-time operational data such as reactor power, neutron flux, and temperature into a dynamic model that would continuously update the WIC based on operational conditions.

Gamma spectroscopy and neutron radiography, in conjunction with ΔT measurements could also be used for more accurate in-core neutron flux data, ultimately reducing uncertainties in the WIC ratio (using He-3 and B10+ detectors). It would also be interesting to extend the WIC estimation method to larger and other reactor types (such as pressured water reactors (PWRs), boiling water reactors (BWRs), and high-temperature gas-cooled reactors (HTGRs)), which would assist in broadening its adoption in the nuclear industry.

References

[1] Natural Resources. Canada, "Government of Canada Advances Small Modular Reactor Research and Development With $13.6-Million Investment." Accessed: Mar. 10, 2025. [Online]. Available: https://www.canada.ca/en/natural-resources-canada/news/2024/10/government-of-canada-advances-small-modular-reactor-research-and-development-with-136-million-investment.html

[2] B. M. van der Ende, L. Li, D. Godin, and B. Sur, "Stand-off nuclear reactor monitoring with neutron detectors for safeguards and non-proliferation applications," *Nat. Commun.*, vol. 10, no. 1, Art. no. 1, Apr. 2019, doi: 10.1038/s41467-019-09967-4.

[3] Canadian Nuclear Laboratories, "CNL completes refuelling of RMC SNOWPOKE-2." Accessed: Jan. 15, 2024. [Online]. Available: https://www.cnl.ca/cnl-completes-refuelling-of-rmc-slowpoke-2-reactor/

[4] J. W. Hilborn, R. E. Kay, P. D. Stevens-Guille, and R. E. Jervis, "SLOWPOKE at the University of Toronto: a laboratory reactor for neutron irradiation," Art. no. AECL--4212, Aug. 1972, Accessed: Mar. 31, 2025. [Online]. Available: https://inis.iaea.org/records/2mg9m-t2t51

[5] J. C. DUCHENSNE, "RMC SLOWPOKE-2 Reactor Thermal Power Determination by Core Water Temperature Measurements.," Master's Thesis, Royal Military College of Canada, Kingston, 1996.

[6] P. Samuleev, "Education and Safety at the SLOWPOKE-2 Facility." Accessed: Mar. 10, 2025. [Online]. Available: https://www.rmc-cmr.ca/en/chemistry-and-chemical-engineering/education-slowpoke-2-facility

[7] F. Puig and H. Dennis, "Neutron fluence effects on SLOWPOKE-2 beryllium reflector composition and reactivity," *Nucl. Eng. Des.*, vol. 305, pp. 4541–460, Jun. 2016, doi: 10.1016/j.nucengdes.2016.05.033.

[8] "tgm-neutron-detectors.pdf." Accessed: Mar. 10, 2025. [Online]. Available: https://web.mit.edu/8.13/www/JLExperiments/38/tgm-neutron-detectors.pdf

[9] A. Soloway, R. Barth, R. Gahbauer, T. Blue, and J. H. J. Goodman, "The rationale requirements for the development of boron neutron capture therapy of brain tumors," *J. Neurooncol.*, vol. 33, pp. 9–18, Jun. 1997, doi: 10.1023/A:1005753610355.

[10] M. D. Di Giovanni, "NEUTRON FLUX AND TEMPERATURE ANALYSIS OF THE SLOWPOKE-2 AND ASSOCIATED CFD MODEL ANALYSE," Royal Military College of Canada, 2023.

[11] ANSYS, "ANSYS Fluent." [Online]. Available: https://www.ansys.com/products/fluids/ansys-fluent

[12] F. Puig and H. Dennis, "Annals of Nuclear Energy SLOWPOKE-2 alternative core loading configurations analysis for highly improved reactor performance," *Ann. Nucl. Energy*, vol. 128, pp. 216–230, 2019, doi: 10.1016/j.anucene.2018.12.016.

[13] "str-375-sg-long-term-r-and-d-plan-2012-2023.pdf." Accessed: May 11, 2023. [Online]. Available: https://www.iaea.org/sites/default/files/19/03/str-375-sg-long-term-r-and-d-plan-2012-2023.pdf

[14] "PicoLog 6 data logging software | Pico Knowledge Base." Accessed: Mar. 31, 2025. [Online]. Available: https://www.picotech.com/library/knowledge-bases/data-loggers/picolog-6-data-logging-software

[15] "The Uses of SOOW Cable - A Complete Guide," Americord. Accessed: Mar. 10, 2025. [Online]. Available: https://www.americord.com/en-ca/blogs/blog/the-uses-of-soow-cable-a-complete-guide

[16] "Heating Element | MNPT 2 in. Electric 3-Phase 6kw 208 x 30 in. Immersion Length - Low 30 Watts / sq. in. - SS316." Accessed: Mar. 25, 2025. [Online]. Available: https://www.glaciertanks.com/heating-elements-bu-elemt-r6kw-208-low.html

[17] D. S. M. FASM Ph D., "Heat treatment of aluminum VI – Artificial aging | Thermal Processing Magazine." Accessed: Mar. 10, 2025. [Online]. Available: https://thermalprocessing.com/heat-treatment-of-aluminum-vi-artificial-aging/

[18] "ANSYS FLUENT 12.0 Theory Guide - 1.2 Continuity and Momentum Equations." Accessed: Apr. 01, 2025. [Online]. Available: https://www.afs.enea.it/project/neptunius/docs/fluent/html/th/node11.htm

[19] "ANSYS FLUENT 12.0 User's Guide - 13.2.4 Natural Convection and Buoyancy-Driven Flows." Accessed: Apr. 01, 2025. [Online]. Available: https://www.afs.enea.it/project/neptunius/docs/fluent/html/ug/node470.htm

[20] "Reynolds' Number - an overview | ScienceDirect Topics." Accessed: Apr. 01, 2025. [Online]. Available: https://www.sciencedirect.com/topics/engineering/reynolds-number

[21] K. Podila, C. Li, C. Azih, and Q. Chen, "Modelling of heat transfer in a molten salt loop using computational fluid dynamics," *Prog. Nucl. Energy*, vol. 164, no. September, p. 104880, 2023, doi: 10.1016/j.pnucene.2023.104880.

[22] "Moist Air - Properties." Accessed: Apr. 01, 2025. [Online]. Available: https://www.engineeringtoolbox.com/moist-air-properties-d_1256.html

[23] Pico Technology, "PicoLog 6 data logging software." Accessed: Jun. 03, 2024. [Online]. Available: https://www.picotech.com/library/data-loggers/picolog-6-data-logger-software

[24] Pico Technology, "Download PicoLog 6." Accessed: Jun. 03, 2024. [Online]. Available: https://www.picotech.com/downloads

[25] G. Albadawi, S. Wang, and X. Cao, "Numerical and experimental study of thermal stratification outside a small SMR containment vessel," *Sustain. Switz.*, vol. 10, no. 7, pp. 1–8, 2018, doi: 10.3390/su10072332.

[26] "ANSYS FLUENT 12.0 Theory Guide - 18.4.3 Pressure-Velocity Coupling." Accessed: Apr. 01, 2025. [Online]. Available: https://www.afs.enea.it/project/neptunius/docs/fluent/html/th/node373.htm

[27] F. P. Incropera, D. P. DeWitt, T. L. Bergman, and A. S. Lavine, Eds., *Fundamentals of heat and mass transfer*, 6. ed. Hoboken, NJ: Wiley, 2007.

[28] T. S. Nguyen, X. Wang, S. Yue, C. R. Atomic Energy of Canada Limited, and C. R. Canadian Nuclear Laboratories, "Validations of gamma measurements in research reactors with MCNP full-reactor models," Atomic Energy of Canada Limited, Chalk River, Ontario (Canada), AECL-CW--123510-CONF-001, Jan. 2016. Accessed: Apr. 10, 2025. [Online]. Available: https://inis.iaea.org/records/jsjx1-19711

[29] T. S. Nguyen, G. B. Wilkin, J. E. Atfield, and C. R. Atomic Energy of Canada Limited, "Monte Carlo calculations applied to SLOWPOKE full-reactor analysis," Atomic Energy of Canada Limited, Chalk River, Ontario (Canada), AECL-CW--123340-CONF-001, Jan. 2012. Accessed: Apr. 10, 2025. [Online]. Available: https://inis.iaea.org/records/6jcpq-har11

Appendix A: Python script

The following code is an example of the power added and lost from the type-K thermocouple data gathered from all 8 channels on the thermocouple array at 8.85 kW nominal reactor power.

```
import numpy as np
import pandas as pd
from scipy import stats

# Load the dataset
df = pd.read_csv("8.85kWRP.csv")

# Convert timestamp to elapsed minutes
df["Time"] = pd.to_datetime(df.iloc[:, 0], format="%H:%M:%S")
start_time = df["Time"].iloc[0]
df["Elapsed (min)"] = (df["Time"] - start_time).dt.total_seconds() / 60

# Define time window to match times
total_duration = df["Elapsed (min)"].max()
end_time = total_duration - 200
filtered_df = df[(df["Elapsed (min)"] >= 25) & (df["Elapsed (min)"] <= end_time)]

# Channels to analyze
channels = filtered_df.columns[3:10]
heating_rates = []

for channel in channels:
    channel_data = filtered_df[["Elapsed (min)", channel]].dropna()
    if len(channel_data) < 3:
        continue

    x = channel_data["Elapsed (min)"].values
    y = channel_data[channel].values.astype(float)
    slope, intercept, r_value, p_value, std_err = stats.linregress(x, y)



# Constants
pi = np.pi
r_water = 1.25  # Radius of the water pool (m)
r_aluminum = 0.425  # Radius of the aluminum cylinder (m)
fuel_bottom = 5.0  # Depth of the bottom of the fuel (m)
specific_heat_water = 4184  # Specific heat capacity of water (J/Kg*C)
density_water = 998  # Density of water (Kg/m^3)
convection_coefficient_water_surface = 10  # Assumed W/m^2*C for natural convection
convection_coefficient_dirt_surface = 5  # Assumed W/m^2*C for dirt surface
thermal_conductivity_concrete = 1.75  # W/m*C
```

```
thermal_conductivity_dirt = 0.5  # W/m*C
thermal_conductivity_stainless_steel = 16  # W/m*C
room_temperature = 19.25584148  # Ambient air temperature (Celsius)
dirt_temperature = 15  # Assumed dirt temperature (Celsius)
thickness_liner = 0.05  # Thickness of the stainless steel liner (m)
thickness_concrete = 0.6  # Thickness of concrete walls (m)
thickness_dirt = 1.0  # Thickness of surrounding dirt (m)
evaporation_velocity = 0.5  # Assumed water velocity at surface (m/s)
humidity_ratio_saturated = 0.02  # Assumed X_s for saturated air
humidity_ratio_air = 0.01  # Assumed X for ambient air

depths = [5.0, 4.5, 4.0, 3.5, 2.5, 1.5, 1.0, 0.5]  # Updated thermocouple locations
slice_heights = [0.5, 0.5, 0.5, 0.5, 1.0, 1.0, 0.5, 0.5]
k = range(0, 8)  # Adjusted indices for 8 thermocouples

# Function to calculate volume
def calculate_volume(depth, slice_height):
    if depth >= fuel_bottom:
        return pi * slice_height * r_water ** 2
    else:
        return pi * slice_height * (r_water ** 2 - r_aluminum ** 2)

# Compute power added based on heating rates
power_added = np.zeros(8)
power_error = np.zeros(8)
power_losses_convection = np.zeros(8)
power_losses_conduction = np.zeros(8)
power_losses_evaporation = np.zeros(8)

for i, (channel, heating_rate, std_err, ci, r_squared) in enumerate(heating_rates):
    volume = calculate_volume(depths[i], slice_heights[i])
    specific_heat = specific_heat_water * density_water * volume
    volume_error = pi * (0.01) * r_water ** 2  # Uncertainty in volume from slice height (±1 cm)
    specific_heat_error = specific_heat * (volume_error / volume)  # Propagate volume uncertainty

    # Compute power added without losses
    power_added[i] = (heating_rate / 60) * specific_heat
    #power_error[i] = np.sqrt(((std_err / 60) * specific_heat) ** 2 + (heating_rate / 60 * specific_heat_error)
** 2)
    power_error[i] = power_added[i] *np.sqrt((std_err/heating_rate) ** 2 +
(specific_heat_error/specific_heat) ** 2)
    # Compute convection losses only for the topmost layer
    print(power_error[i])
    if i == 0:
        surface_area = 2 * pi * r_water * slice_heights[i]
        avg_water_temp = filtered_df[channels[i]].mean()
        power_losses_convection[i] = np.abs(convection_coefficient_water_surface * surface_area *
(avg_water_temp - room_temperature))
        #print(power_losses_convection)
```

```
    # Compute conduction losses with proper heat resistance calculations
    surface_area_liner = 2 * pi * (r_water + thickness_liner) * slice_heights[i]
    surface_area_concrete = 2 * pi * (r_water + thickness_liner + thickness_concrete) * slice_heights[i]
    surface_area_dirt = 2 * pi * (r_water + thickness_liner + thickness_concrete + thickness_dirt) *
slice_heights[i]

    r_liner = thickness_liner / (thermal_conductivity_stainless_steel * surface_area_liner)
    r_concrete = thickness_concrete / (thermal_conductivity_concrete * surface_area_concrete)
    r_dirt = thickness_dirt / (thermal_conductivity_dirt * surface_area_dirt)
    r_in = 1 / (convection_coefficient_water_surface * surface_area_liner)
    r_out = 1 / (convection_coefficient_dirt_surface * surface_area_dirt)
    r_sum = r_liner + r_concrete + r_dirt + r_in + r_out

    power_losses_conduction[i] = (avg_water_temp - dirt_temperature) / r_sum
    #print(power_losses_conduction)
    # Compute evaporation losses only for the topmost layer
    if i == 0:
        power_losses_evaporation[i] = (25 + 19 * evaporation_velocity) * surface_area *
(humidity_ratio_saturated - humidity_ratio_air)
       # print(power_losses_evaporation)

sumP = np.nansum(power_added)
#print(power_added)
sumE = np.nansum(power_error)
sumL_losses =  np.sum(power_losses_convection) + np.sum(power_losses_conduction) +
np.sum(power_losses_evaporation)
net_power = sumP - sumL_losses

print("The estimated power added to the pool (without losses) is:", sumP, "+/-", sumE, "Watts")
print("The net power added to the pool is:", net_power, "+/-", sumL_losses, "Watts")
```

Appendix B: Supporting Figures and Tables

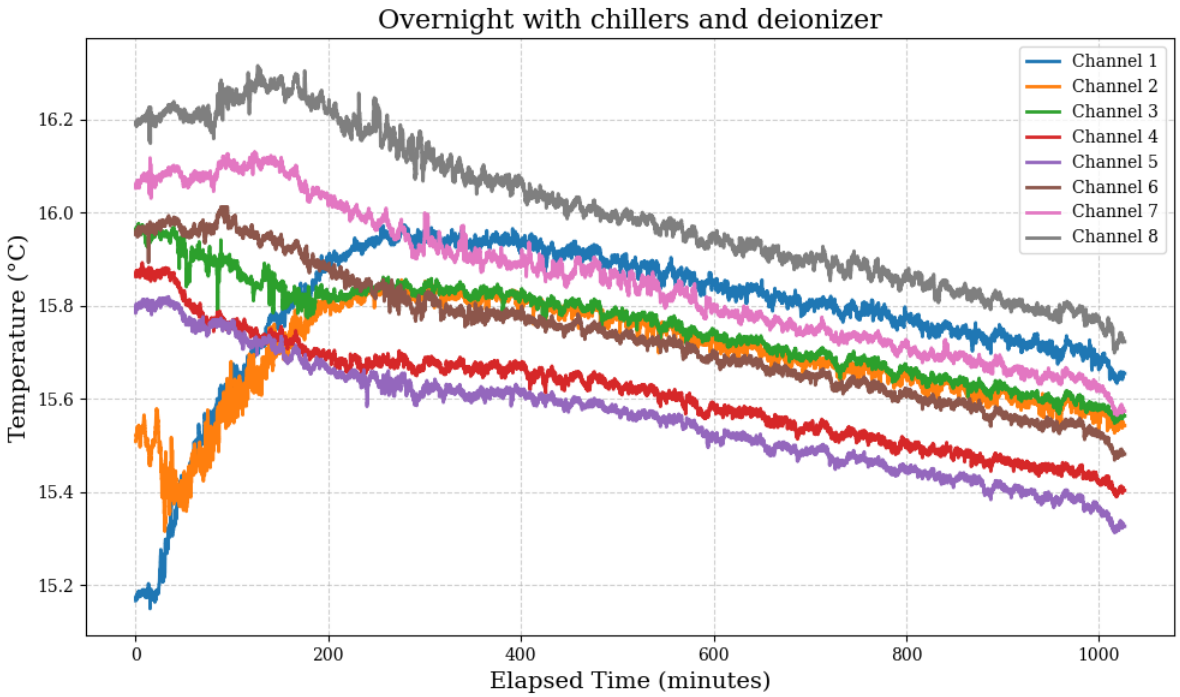

Figure 45: Effect of deionizer on Channel 1 and Channel 2 (Deepest channels near the deionizer).

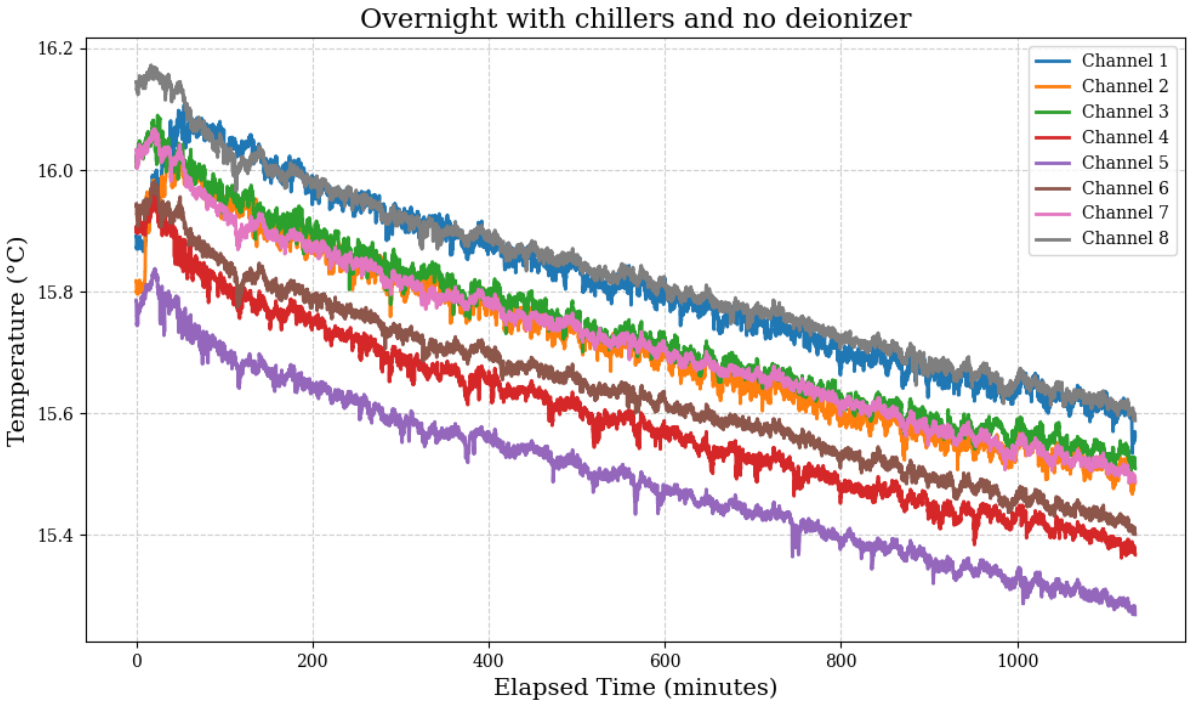

Figure 46: Temperature data from all 8 thermocouples with chillers turned on overnight.

Table 15: Neutron flux average counts per min (CPM) for B10+ and He-3 detectors, as well as ΔT between inlet and outlet thermocouples displayed on SIRCIS.

			B10+		He-3		ΔT (°C)	
Date (2023)	Time (HH: MM)	Flux n/ cm^2)	Average	Stdev of mean	Average	Stdev of mean	Average	Stdev of mean
19-Oct	10:42-15:31	5.00E+11	93.06	2.31	292.44	20.41	14.216	0.005
23-Oct	15:23-15:53	2.50E+10	20.80	3.18	77.26	51.97	10.924	0.010
25-Oct	10:38-15:34	3.00E+10	11.01	6.78	26.70	12.82	3.065	0.001
07-Nov	9:33-10:42	5.00E+11	22.50	29.16	46.75	37.99	15.871	0.012
08-Nov	10:42-15:31	1.00E+12	174.93	19.21	401.23	50.56	21.217	0.008
23-Oct	15:01-15:03; 15:54-16:11	5.00E+11	22.47	39.00	15.93	78.00	9.355	0.025
07-Nov	10:43-15:39	1.00E+12	171.46	14.44	481.80	18.54	21.053	0.007

Table 16: Mean ΔT before and after refuelling that occurred in Sept 2021 [2].

Date	Mean (°C)	Standard Deviation (°C)	Number of Points	Standard Deviation of the Mean (°C)
2021-06-30	15.252	±0.572	19,130	±0.004
2021-12-08	14.651	±0.622	13,125	±0.005

Table 17: Mean CPM using both B10+ and He-3 neutron flux detectors before and after refuelling [2].

Date Range	Number of Events at 5 x 10^{11} n/cm^2-s	Detector	Mean (cpm)	Standard Deviation (cpm)	Standard Deviation of the Mean (cpm)
2021 April 22-August 19	37	B10+	12.3	±2.4	±0.4
		He-3	29.8	±10.1	±1.6
2021 May 12 – August 19	32	He-3	31.2	±10.2	±1.8
2021 September 14 – 2022 May 5	65	B10+	11.64	±1.53	±0.19
		He-3	29.5	±4.0	±0.5